

# Origin of internal flow structures in columnar-jointed basalt from Hrepphólar, Iceland: I. Textural and geochemical characterization

Sonja A. Bosshard · Hannes B. Mattsson · György Hetényi

Received: 21 September 2011 / Accepted: 14 May 2012 / Published online: 13 June 2012  
© Springer-Verlag 2012

**Abstract** Basalt columns from Hrepphólar (Iceland) show distinct internal structures produced by alternating brighter and darker bands through the column, locally exhibiting viscous fingering features. Here, we present geochemical and petrographic data retrieved from analyses of major and trace elements and mineral chemistry from a cross section of a single basaltic column. This is combined with petrographic descriptions and data on crystal size distributions of plagioclase. We use our data from Hrepphólar to test four existing models that have been proposed to explain banded structures inside columns: (1) deuteric alteration, (2) double-diffusive convection, (3) constitutional supercooling, and (4) crystallization-induced melt migration. We find that the internal structures at Hrepphólar represent primary magmatic features, because approximately 20 % of the observed structures crosscut the column-bounding fracture for each meter along the main axis of the column. These features must thus have been formed before the column-delimiting crack advanced. Major and trace element analyses show small but significant variations across the column and strong correlation between oxides like FeO and TiO<sub>2</sub>, as well as K<sub>2</sub>O and P<sub>2</sub>O<sub>5</sub>. The geochemical variations correlate with the presence of darker/brighter bands visible on a polished surface and can be explained by a variation in the modal

proportions of the main phenocryst phases (specifically variable plagioclase and titanomagnetite content). This banding enhances the internal structures apparent in the polished cross section from columnar joints at Hrepphólar. The measured variations in major and trace element geochemistry, as well as mineral chemistry, are too small to distinguish between the proposed band-forming models. Plagioclase crystal size distributions, however, display a systematic change across the column that is consistent with late-stage migration of melt inside the column (i.e., the crystallization induced melt migration hypothesis). The central part of the columns have plagioclases indicative of slow cooling and these are also more steeply oriented (i.e., subparallel to the column axis) compared with plagioclases present in the more rapidly cooled edges. This redistribution of melt within individual columns may significantly affect the cooling rate of columnar-jointed lava flows and intrusions.

**Keywords** Columnar jointing · Hrepphólar · Iceland · Melt migration · Crystal size distribution · Magmatic banding

## Introduction

Columnar-jointed rock has for a long time fascinated observers with its regular, and often spectacular, hexagonal patterns. The earliest scientific descriptions in literature date back to the seventeenth century (Bulkeley 1693). Since then, many workers have provided detailed descriptions of the arrangements of columnar joints and offered various hypotheses on their formation (Tomkeieff 1940; Spry 1962; Ellwood and Fisk 1977; Budkewitsch and Robin 1994; Grossenbacher and McDuffie 1995; Goehring and Morris 2005; Gilman 2009; Guy 2009). Columnar joints are a common feature in subaerial lava flows, especially of

Editorial responsibility: A. Gudmundsson

S. A. Bosshard (✉) · H. B. Mattsson (✉) · G. Hetényi  
Institute of Geochemistry and Petrology,  
Swiss Federal Institute of Technology (ETH Zürich),  
Clausiusstrasse 25,  
8092 Zurich, Switzerland  
e-mail: sonja.bosshard@erdw.ethz.ch  
e-mail: hannes.mattsson@erdw.ethz.ch

G. Hetényi  
Swiss Seismological Service (ETH Zürich), Sonneggstrasse 5,  
8092 Zürich, Switzerland

basaltic composition but can also be found in lava flows of other compositions such as andesites, rhyolites, and obsidians (Spry 1962), as well as in densely welded pyroclastic rocks (Fritz and Stillman 1996; Michol et al. 2008). Although many previous studies have focused on the processes of columnar joint formation and the propagation of column-delimiting joints, only a few studies have in detail described the small-scale variations occurring within individual columns (Ellwood and Fisk 1977; Ellwood 1979).

Several previous studies have described diffuse, near-circular banding which can be observed when columns are cut perpendicular to their long axes (Kantha 1981; Mattsson et al. 2011). In literature, four different models have been proposed to explain these internal structures: (1) deuteric alteration due to flow of water along fractures (Smedes and Lang 1955), (2) double-diffusive convection and viscous fingering (Kantha 1981), (3) constitutional supercooling (Guy and Le Coze 1990; Gilman 2009; Guy 2009), and (4) crystallization-induced melt migration (Mattsson et al. 2011). Although the models span a wide variety of different physical processes, they could all potentially produce the observed semi-circular structures. However, these models are mainly theoretical and little direct evidence has been presented to support the proposed processes. Therefore, this study aims to provide detailed petrographic, mineralogical, and geochemical data from a continuous section through one basaltic column from Hrepphólar (southern Iceland).

In southern Iceland, numerous interglacial lava flows have been emplaced on top of a tilted Plio-Pleistocene succession of lava flows intercalated with hyaloclastites and tillites (i.e., the Hreppar Series; Saemundsson 1970). Many of these flat-lying interglacial lava flows have developed columnar joints, and the Hrepphólar lava flow has been interpreted as being ponded in topographic

low, which allowed for development of long slender columns under static conditions (Saemundsson 1970). The columns are nicely exposed in outcrops at Örmhóll and Hólahnúkar (where they are also mined), approximately 1 km east of the Hrepphólar farm (Fig. 1a, b). The Hrepphólar columns measure on average 0.45 m in diameter (Kristinsdóttir 2010), and many columns exceed 20 m in length (the lower contact of this lava flow is not exposed so the total thickness is unknown; Fig. 1b). In cross section, the Hrepphólar basalt columns display distinct internal structures and they are therefore excellent candidates to test which geochemical and petrographic approaches record most information related to the origin of these features. The same basalt column is also analyzed for its rock magnetic properties and anisotropy of magnetic susceptibility (AMS) in an accompanying paper (Almqvist et al. 2012). In combination, these two studies provide a comprehensive data set from a single basalt column. Such data are essential to properly evaluate and test the different models that have been suggested to produce the internal structures in basalt columns.

In order to characterize the textural and geochemical variations through a single column, we used a number of complementary analytical techniques. We measured the bulk-rock geochemistry, mineral compositions, 2D orientation of plagioclase laths as well as stereologically corrected crystal size distributions of plagioclase, from a continuous profile across one of these columns. We infer that the observed structures are primary magmatic features formed during cooling and solidification of the Hrepphólar lava flow. Finally, we evaluate which information can be retrieved from systematic studies of small-scale structures in columnar-jointed basalts and how these data fit with the different proposed hypothesis for the origin of viscous fingering and diffuse semi-circular banding in basalt columns.

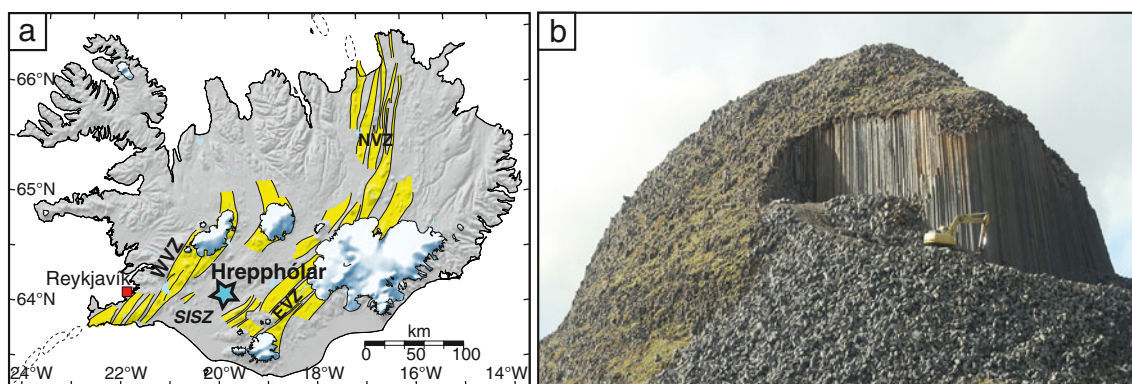


**Fig. 1** **a** Map showing the location of Hrepphólar in relation to the currently active and overlapping spreading zones in southern Iceland (i.e., the Western and Eastern Volcanic Zone, WVZ and EVZ, respectively, as well as the South Iceland Seismic Zone). **b** Photograph

showing the active quarry at Hólahnúkar, approximately 1 km east of the Hrepphólar farm. Excavator gives scale. Photograph courtesy of Sverrir Þórolfsson

### Background: existing genetic models for the development of internal structures in basalt columns

The development of internal structures and banding inside basaltic columns has been proposed to be the result of widely different physical and chemical processes. In this section, we briefly review different models from the literature which we later compare the results from our study with those of the existing models. It is important to note that one model involves no movement of melt inside the columns (deuteric alteration), two models (double-diffusive convection and to a lesser degree also constitutional supercooling) involve convective movement of material and that none of the models account for volume loss during solidification (therefore the amount of material upwelling must be equal to the amount of downwarped material in order to maintain a constant volume of the lava flow). The fourth and last model (crystallization-induced melt migration) involves unidirectional movement of molten material in side columns as a result of continuous decrease in the specific volume during crystallization within the central part of the column.

#### Deuteric alteration

Deuteric alteration involves flow of meteoric or hydrothermal waters inside the free space created by the column delimiting joints (Fig. 2a, b), and this process has been invoked to explain semi-circular structures observed in columnar-jointed basalts (i.e., Smedes and Lang 1955). The change in color and development of internal banding inside columnar basalt from southwestern Oregon was interpreted to result from systematic leaching of different elements in combination with hydration of glass groundmass (i.e., palagonitization) which can generate a darker rim compared with a lighter-colored core (Smedes and Lang 1955). In the columns studied by Smedes and Lang (1955), the authors observed nearly identical mineral chemistry and crystal sizes from the rim to the core of the column. However, towards the edges of the column they noted alteration of magnetite and glass to form limonite, whereas the compositions of plagioclase crystals remained largely unaffected by the alteration process. In general, deuteric alteration of basaltic lavas involves iddingsite formation around cracks and rims of olivine crystals as well as leaching and hydration of interstitial glass with subsequent precipitation of various low-temperature zeolites (e.g., Juteau et al. 1979; Kristmannsdottir 1979; Andrews 1980; Shelley 1993; Alt et al. 1996; Schenato et al. 2003). These mineralogical changes are also likely to produce a slight change in bulk geochemistry of the affected rock. This should result in a systematic compositional variation between the edges and the central parts in the columns, whereas the main petrographic textures should not significantly change with position in the column. The

semi-circular pattern is in this case thought to develop from overlapping areas near intersecting column edges, and this may explain why bands become progressively more rounded in the internal parts of the columns (Fig. 2a, b).

#### Double-diffusive convection and constitutional supercooling

Kantha (1981) proposed the double-diffusive convection model to explain the internal structures as well as the overall mechanism behind formation of columnar joints in basaltic lavas. In his study, Kantha (1981) compares the internal structures observed in basalt columns with analogous experiments done using hot salty water and cold fresh water. If cold, fresh water lies above warmer salty water, the fluids are initially stable. However, the heat loss from the lower (hotter) fluid is much quicker than the rate of salt diffusion between the fluids, which leads to oscillatory movements and subsequently also development of double-diffusive interfaces which can form “salt fingers” rising into the less saline fluid (Kantha 1981 and references therein). The process is not limited to systems where there are differences in salinity and temperature; any two solutions with similar diffusivities can produce such structures (Turner 1973). Kantha (1981) argued that in the case of a basaltic magma an early developed thermal structure can be perturbed by instabilities arising from differences in heat and composition. For example, if there is a hotter part of a basalt, enriched in heavy chemical components and overlying slightly colder material with less of this chemical component, the overall system appears to be stable, but some instabilities would develop and result in basalt fingers (Kantha 1981). Ultimately, the double-diffusive convection and fingering results in a three-layered structure with a strong convection in the center of the fluid, whereas the lower and upper layers become finger regions (Kantha 1981). Kantha (1981) compares this structure with the typical structure of an ideal columnar-jointed lava flow, comprising upper and lower colonnades with the entablature in between (as described by Spry 1962). Thus, in the model proposed by Kantha (1981), basalt fingers are driven by the difference of composition and heat across a vertical profile of the lava flow, and therefore it also follows that there should be a systematic difference in composition from the top to the bottom of a columnar-jointed lava flow as well as from the edges to the centre of each column. Several workers have demonstrated geochemical differences between the entablature and the colonnades (e.g., Spry 1962), but no clear systematic geochemical trend has hitherto been reported from the edge to the centre of a single column.

Another process that has been proposed in order to explain both the internal structures inside basalt columns as well as controlling where column-bounding cracks develop

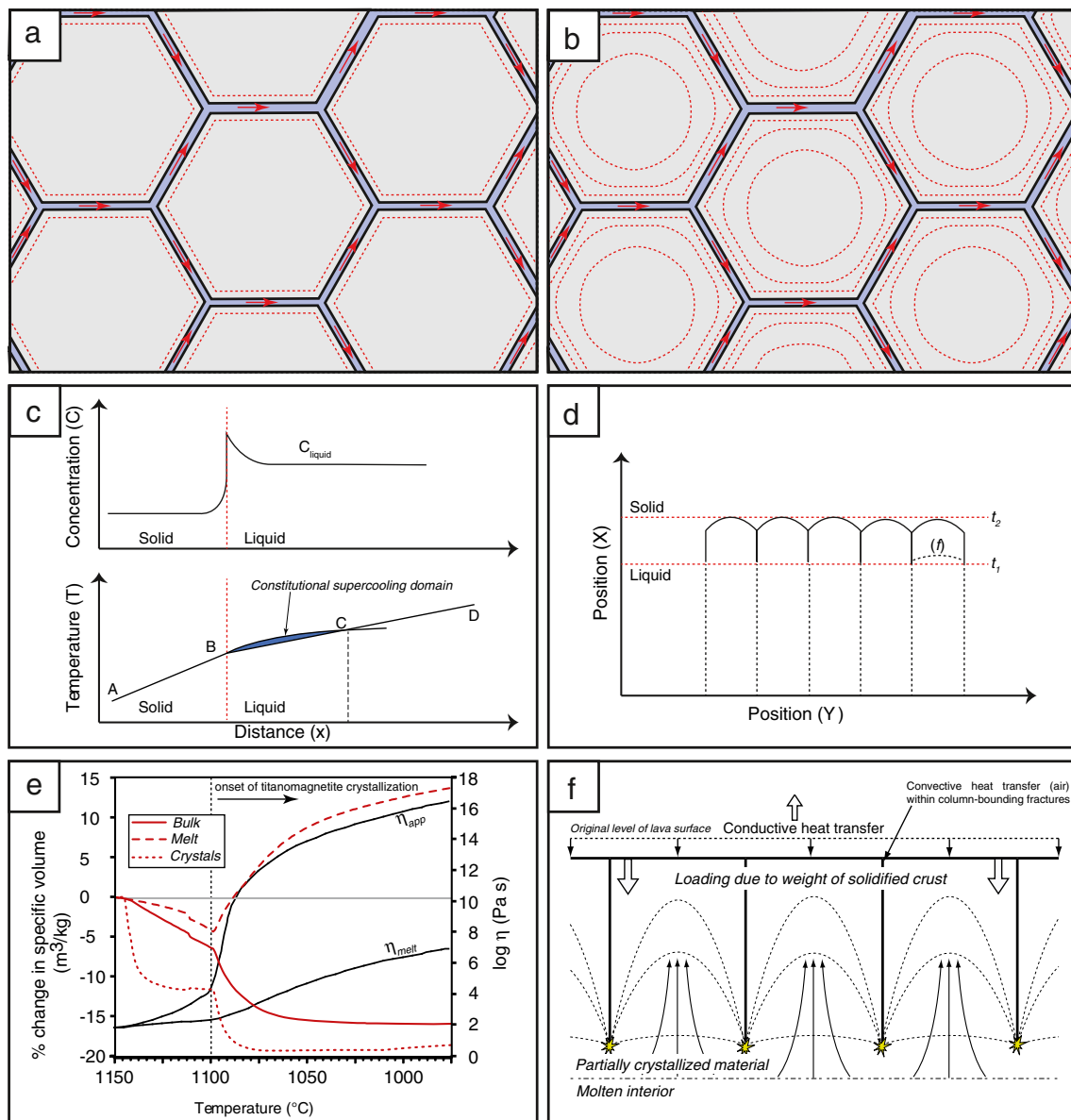


**Fig. 2** Schematic illustrations of the different models proposed to explain internal structures in basalt columns. *Deuteric alteration*: **a** a water is circulating in the column delimiting cracks after emplacement and systematically leaches elements out of the column, starting from the sides and progressing inwards. **b** As time progresses, the leaching is affecting deeper into the columns and the overall shape of the leaching front becomes progressively more rounded towards the central parts. *Double-diffusive convection and constitutional supercooling*: **c** (upper) progressive solidification preferentially enriches some elements in the liquid phase producing a compositional contrast between solid and liquid ( $C_{\text{solid}}$  and  $C_{\text{liquid}}$ , respectively).  $X$  denotes an arbitrary distance from the cooling surface. **c** (lower) Temperature profiles across the liquid–solid interface. The temperature profile consist of two straight lines (AB and BD) imposed by thermal diffusion. The curved line (BC) denotes the liquidus temperature that corresponds to the composition of the liquid and this varies in space depending on expulsion of a solute. The blue field which outlines the area where the liquidus temperature is greater than the local temperature represents the constitutional

supercooling domain of Guy and Le Coze (1990). **d** Instability of a planar surface interface. Time  $t_1$  displays a mean planar interface as well as a heterogeneity ( $f$ ) with respect to the planar surface. The supercooling domain spreads from ( $t_1$ ) up to ( $t_2$ ). The growth rate of the solid is greater on the top of the bump than laterally. This heterogeneity is amplified until it reaches plane ( $t_2$ ). *Crystallization-induced melt migration*: **e** thermodynamic modeling of the Hrepphólar system shows that crystallization of titanomagnetite produces a large drop of the specific volume during solidification. At the same time as the drop of the specific volume occurs, the viscosity of the system ( $\eta_{\text{app}}$ =crystals+melt) increases rapidly relative to the melt. This suggests that it is easy to move melt through a partially crystallized framework to accommodate the volume decrease. **f** The source of the migrating molten material is located near the interface of liquid and partially crystallized material. The net effect of the melt migration into the columns is an overall lowering of the upper surface of the lava flow; **c**, **d** redrawn from Guy and Le Coze (1990) and **e**, **f** modified from Mattsson et al. (2011)



and propagate is the constitutional supercooling model (i.e., Guy and Le Coze 1990; Gilman 2009; Guy 2009). The process of constitutional supercooling is well known from metallurgy, where, if an impurity is present in an alloy, it will not remain stable (i.e., non-planar conditions between crystals and melt, Glicksman 2011). Although the cooling of metal alloys is predominantly on a microscopic scale, a similar process has been invoked for large-scale cooling of basaltic lava flows (Guy and Le Coze 1990; Gilman 2009; Guy 2009).

Overall, the constitutional supercooling model (Fig. 2) is similar to the double-diffusive convection model originally proposed by Kantha (1981). This is mainly due to the fact that both models require gradients in heat and composition during the cooling/solidification process to generate surface instabilities. There are some subtle differences in the two proposed constitutional supercooling models. Gilman (2009) argued that the early solid which crystallizes from basalts consists of minerals with a high melting point, such as aluminates, whereas the last crystallized minerals have a considerably lower melting-point like for example silicates. Thus, if this process was in fact responsible for the formation of basalt columns there would also be a compositional gradient from the edges to the centre of the individual columns. Guy and Le Coze (1990) and Guy (2009) argued that the compositional differences in silicate systems, in terms of major elements, are not sufficient to produce the necessary contrast in concentration (since most minerals have overlapping crystallization sequences and include many of the major elements into their crystal structure). Instead, it was argued by Guy and Le Coze (1990) and Guy (2009) that the compositional contrast driving this process may instead have been the volatile content (e.g., H<sub>2</sub>O), which becomes progressively more enriched in the melt as the solidification process continues.

#### Crystallization-induced melt migration

Mattsson et al. (2011) recently proposed a physical model for melt migration in basalt columns driven by the continuous decrease of specific volume inside the solidifying columns (Fig. 2e, f). In their paper (Mattsson et al. 2011), the authors argue that when a columnar-jointed lava flow starts to solidify, the heat loss is dominated by conductive heat transfer to the air above the lava flow, while isotherms inside the lava flow are nearly horizontal. However, as cooling and solidification continues and column-delimiting joints propagate inward the heat loss to the sides of the column becomes locally dominant (Fig. 2f). This results in a steepening of isotherms inside the columns. Solidification of basaltic lavas is associated with a 10–15 % decrease in specific volume and this loss has to be accounted for in some way (Boudreau and Philpotts 2002; Mattsson et al.

2011). Typically, the free space created by the jointing itself can only account for maximum a few percent of this volume. By using thermodynamical modeling Mattsson et al. (2011) showed that crystallization of titanomagnetite results in a significant drop in specific volume coupled to a drastic increase in viscosity of the bulk system (Fig. 2e). The continuous volume decrease is accommodated by sinking of the solidified top and fracture area while the still molten material is migrating upwards into the central part of the columns (Fig. 2f). The overall subsidence of the upper surface of the lava flow accounts for the predicted 15 % volume decrease during solidification. It is important to note that this model involves unidirectional movement of material in the columns over a relatively short distance and only applies to internal structures (i.e., it does not explain the origin of the columnar jointing itself).

## Methods

### Samples and profiles

Basalt columns from Hrepphólar display distinctly banded features in cross section. Because of the internal banding these columns are mined as ornamental building stones and can be found as floor tiles in various public buildings in Iceland. For example, most of the floor tiles in the departure hall of Keflavík international airport show identical features as those described here. Therefore, although we only investigate one polished slab in detail, it is clearly representative of the Hrepphólar columns. In order to document and characterize small-scale geochemical and textural variations occurring within a single column, we used a polished slab of a column (30 cm wide and 55 cm high; Fig. 3c). This sample represents a central section along the long-axis of a column where the most prominent internal features are located (Fig. 3). Because the polished plate is cut on the sides to make a rectangular tile, it is difficult to estimate exactly how much material is missing on either side of the sample (i.e., the distance from the edge of the tile to the edge of the column), and if this is asymmetrically oriented or not. However, we know from the sizes of the mined columns that the longest cross-sectional distance measured within a single column is approximately 0.45 m (leaving ~7.5 cm on each side unaccounted for in our sample). We also know from other polished slabs that the most prominent internal features are typically found in the central parts (similar to that observed in our plate; Fig. 3), therefore, it is likely that the asymmetry is minor. From our polished slab, we cut several profiles in order to prepare thin sections (samples marked LS1 to LS20, with a size of 2×2.5×1 cm each, cut parallel to the slab surface; Fig. 3a) and material for geochemical analyses (cubes A1 to A27 with a size of 1×1×1 cm each;

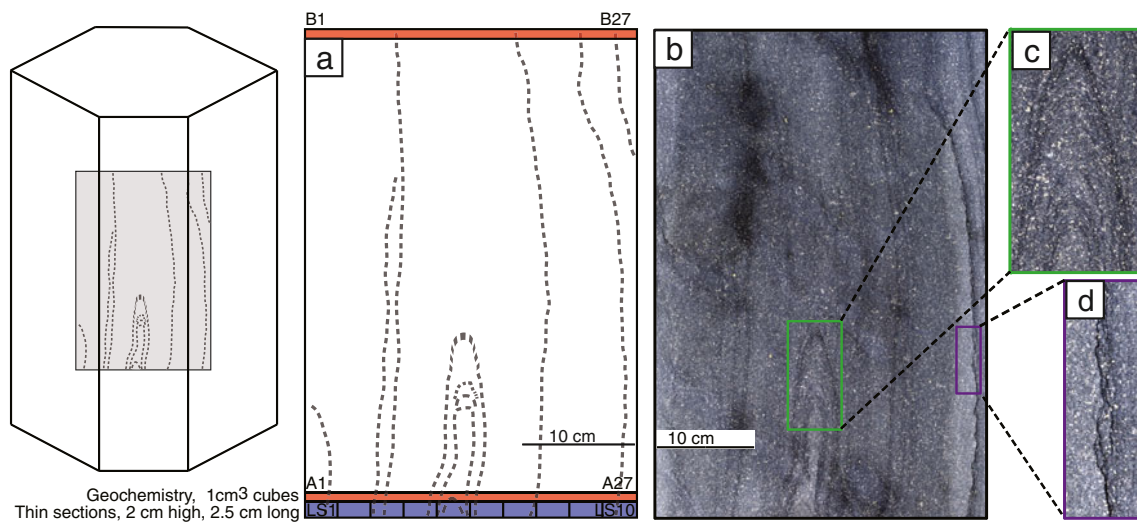


**Fig. 3** Sketch of the Hrepphólar columnar basalt together with examples of the internal structures that can be observed. **a, b** Photograph and simplified sketch showing the main features of internal structures of the studied column. The *blue parts* mark the areas where samples have been cut for thin sections (LS1–10), and the *red parts* correspond to the

profile sampled for AMS (A1–27 and B1–27) and XRF analysis (A1–27). There are two different styles of dark banding present in the columns. **c** Diffuse banding near the centre of the column, and **d** sharp lines/bands that crosscut the diffuse banding

Fig. 3a). Before crushing the cubes for X-ray fluorescence (XRF) and laser ablation inductively coupled plasma mass spectroscopy (LA-ICP-MS) analysis, the cubes were measured for their rock magnetic properties and AMS.

#### Analytical methods

Traditional optical microscopy of thin sections was used to determine mineral assemblages in the samples. The thin sections were photographed at  $\times 2$  magnifications, and the photographs were later used to measure 2D orientation of the long axes of plagioclase laths and to establish crystal size distributions (CSDs).

The outlines of 10,208 plagioclase crystals were traced by hand from the photographs of thin sections LS1 to LS10 (Fig. 3a) using Adobe Illustrator CS3. This yields an average number of more than 1,000 crystals measured per thin section, which is significantly more than the minimum number of 250–300 crystals required to obtain statistically relevant results (Mock and Jerram 2005; Morgan and Jerram 2006). After tracing the outlines, the image file was converted to a binary TIFF file with ImageJ 1.41o (Rasband 2008). The CSD slice spreadsheet (Morgan and Jerram 2006) was used to estimate values for the short, intermediate, and long axes. The spreadsheet compares the 2D data of intersections to a database and gives an objective estimate of the 3D habit of crystals, defined by a least-square fit of an ellipse and returns the best fit. The crystal size distributions were calculated using the short-intermediate long axis ratios retrieved from the CSD slice spreadsheet and the CSD corrections software (Higgins 2000). The calculated CSD

volume fractions range from 180 to 212 % of the measured 2D values. However, the 2D and CSD-calculated data for the plagioclase is rather well correlated ( $R^2=0.65$ ) indicating that the crystal shapes obtained from the CSD slice spreadsheet, and later used in CSD corrections, yield a reliable volume fraction of crystals (see also Brugger and Hammer 2010).

The cubes from profile A (Fig. 3a) were crushed and ground in an agate mortar into a homogeneous, fine-grained ( $<5 \mu\text{m}$  size) powder, fused with  $\text{Li}_2\text{B}_4\text{O}_7$  and cast into glass pills. Major elements were measured by wavelength dispersive XRF spectrometer (Axios, PANalytical) and trace elements by LA-ICP-MS with a laser from Lambda Physik Complex Pro. The data were processed using the MatLab-based program SILLS v1.0.6 (Guillong et al. 2008). Mineral chemistry was measured using an electron microprobe (JEOL JXA-2800) with an accelerating voltage of 15 kV, a current of 20 nA, and a focused beam. Bulk magnetic susceptibility was measured for profile A (Fig. 3a) using a low-field AGICO KLY2 Kappabridge from the Earth and Planetary Magnetism group at ETH Zürich.

## Results

### Petrography

One of the most striking macroscopic features that can be observed in the Hrepphólar columns is the presence of two different styles of dark banding. Near the center of the plate (Fig. 3c), banding tends to fade out towards the center (i.e.,



diffuse banding). This is in rather sharp contrast to a very dark band/line which shows a well-defined (1–2 mm width) boundary towards the surrounding rock (Fig. 3d). The latter often crosscuts the structures formed by the diffuse bands. In thin section the basalt column from Hrepphólar is relatively fine grained (seriate textured) with plagioclase, clinopyroxene, titanomagnetite/ilmenite phenocrysts with minor amounts of olivine ( $\leq 10$  modal%). The sizes of the phenocrysts range from 0.2 to 1.5 mm (Fig. 4). The groundmass of all samples contains variable amounts of clinopyroxene, plagioclase, and titanomagnetite/ilmenite.

Plagioclase (commonly lath shaped) is the most abundant mineral in the thin sections and ranges in size from 0.2 to 1.5 mm. Some of the larger phenocrysts are not as elongated as the smaller crystals and show clear zonation (Fig. 4c) combined with distinct polysynthetic twinning. However, only a few of these large crystals can be found per thin

section and the bulk of the plagioclase crystals show nearly identical crystal shapes. Discontinuous plagioclase chains (similar to those described by Philpotts et al. 1998, 1999) are also visible in the thin sections. These plagioclase chains do not persist through the whole thin sections (typical lengths of 1 to 1.5 cm can be observed). Near-euhedral olivine (0.5 to 1 mm in size) is much less common than plagioclase but can be found in all thin sections (Fig. 4b). Clinopyroxene is the most abundant mineral in the groundmass and often forms glomerophytic clusters together with plagioclase (Fig. 4a). The clinopyroxene phenocrysts typically range in size from 0.3 to 0.7 mm. Titanomagnetite, which is present in all thin sections, occurs as euhedral crystals varying in size between 0.05 and 0.2 mm (Fig. 4d). Towards the central part of the column, some titanomagnetite display distinctly more elongated, needle-like, shapes (see also Fig. 3 in Almqvist et al. 2012). Modal

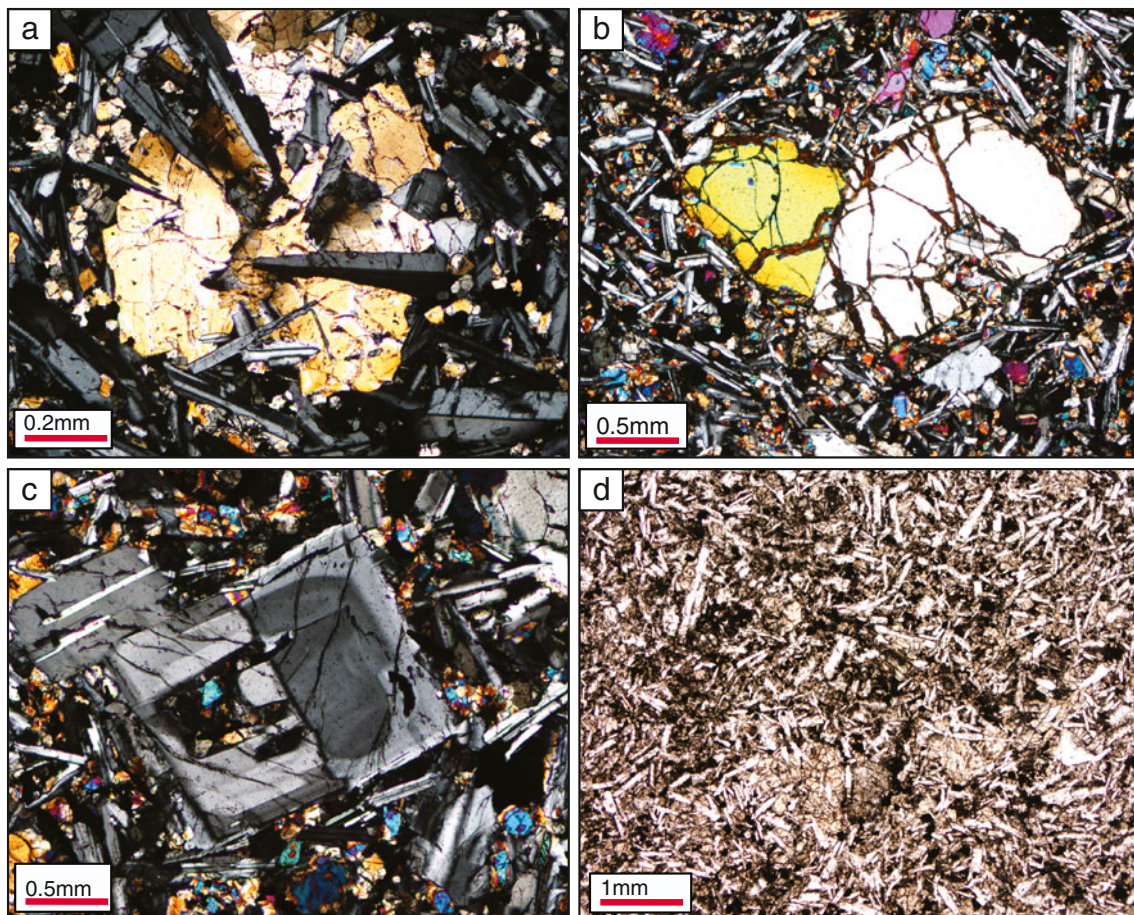


**Fig. 4** Photographs of thin sections showing the main petrographic features observed in the studied column. **a** Clinopyroxene phenocryst (yellow/orange color), approximately 1 mm in size, occurs intimately associated with plagioclase (grey/black) in cross-polarized light. **b** Iddingsite alteration (dark red) along microcracks in a euhedral olivine crystal (cross polarized light). **c** Plagioclase phenocryst with distinct zonation, the quadratic shape is typical for large plagioclase phenocrysts.

The plagioclase shows small intergrown minerals of clinopyroxene from the groundmass (cross-polarized light). **d** Photographs showing the general (seriate) texture of the Hrepphólar basalt. Bright elongated minerals are plagioclase laths, the light brown minerals are clinopyroxene and the black minerals are titanomagnetite (plane polarized light). Note that, although not very distinct, the titanomagnetite tends to form bands, or trails, through the thin section. Note also elongated ilmenite crystals

analyses show that the dark diffuse banding is predominantly a result of the amount of titanomagnetite which is on average 7 modal% in the dark bands, whereas brighter bands contain 4 modal%. Local enrichments of titanomagnetite are visible as darker discontinuous bands in the thin sections (Fig. 4d). Ilmenite can be found as occasional single crystals in the fine-grained groundmass. Overall, the Hrepphólar columns are fresh as indicated by the very minor iddingsite alteration occurring: (1) along cracks or (2) at the outer rims of a few olivine crystals (Fig. 4b).

## Geochemistry

### Major elements

Major element geochemistry data for the samples belonging to Profile A (Fig. 3a) are listed in Table 1. It is clear from the bulk-rock compositions (Table 1) that the Hrepphólar lava has a rather evolved tholeiitic composition with Mg# ( $\text{Mg\#} = \text{Mg}^{2+}/(\text{Mg}^{2+} + \text{Fe}^{2+})$ ) ranging from 24.8 to 26.5 within the column. The major elements are plotted against  $\text{K}_2\text{O}$  as a fractionation index for the present study (Fig. 5) because none of the main phenocryst phases in the samples incorporate significant potassium into their crystal structure. The  $\text{K}_2\text{O}$  content of the samples ranges from 0.41 to 0.46 wt.% (Table 1).  $\text{P}_2\text{O}_5$  shows a distinct positive correlation with  $\text{K}_2\text{O}$ , whereas MgO and CaO correlate negatively. The  $\text{Na}_2\text{O}$ -content remains relatively stable between 2.40 and 2.48 wt.% with increasing  $\text{K}_2\text{O}$ . The remaining oxides (i.e.,  $\text{SiO}_2$ ,  $\text{Al}_2\text{O}_3$ , and  $\text{Fe}_2\text{O}_3$ ) show broad scatter against  $\text{K}_2\text{O}$ . Figure 5 shows that the composition of the bulk rock compositions of individual samples is strongly dependent on the relative fractionation/accumulation of the main mineral phases present in the Hrepphólar columns.

When plotted as a function of their location within the column (A1 to A27), the major elements show a series of positive and negative peaks (Fig. 6). For example  $\text{SiO}_2$  shows three distinct negative peaks in sample A9, A23, and A24. The general  $\text{Al}_2\text{O}_3$  concentration decreases from A1 to A27, although there are some higher peaks. In contrast to the other samples, sample A5 shows in many major element plots a clear positive peak (i.e.,  $\text{K}_2\text{O}$ ,  $\text{P}_2\text{O}_5$ ,  $\text{Na}_2\text{O}$ , and MnO), and a negative peak in CaO and MgO. Samples A23 and A24 are depleted in  $\text{SiO}_2$  and  $\text{Al}_2\text{O}_3$  but in contrast to this, these two samples are enriched in  $\text{Fe}_2\text{O}_3$  and  $\text{TiO}_2$ . Overall,  $\text{Fe}_2\text{O}_3$  and  $\text{TiO}_2$  show a strong covariance across the column (Fig. 6) as does  $\text{K}_2\text{O}$  with respect to  $\text{P}_2\text{O}_5$  (with a high peak in sample A5 and rather low peaks in samples A3 and A23). The negative correlation between  $\text{Fe}_2\text{O}_3$  and  $\text{Al}_2\text{O}_3$  (Fig. 6) strongly indicates variable proportions of titanomagnetite and plagioclase respectively, between different samples.

### Trace elements

All analyzed samples from Profile A have similar trace element concentrations (Table 1). In order to illustrate the variation in trace elements across the column we have chosen to plot five representative samples (i.e., A1, A5, A17, A20, and A27), one from each edge of the polished plate and three additional samples which represent the total measured variation. The trace element concentrations display less scatter than the rare earth elements (REE) concentrations and all five samples plot close to one another (Fig. 7). Although there is some scatter in the concentration of the REE between the representative samples, all analyzed samples are characterized by relatively high  $(\text{La}/\text{Yb})_N$  ratios ranging between 2.96 and 3.51 (Fig. 7; Table 1). In order to further identify the causes of geochemical variations across the column, we also normalized the representative samples to the average composition ( $n=27$ ) of the column (Fig. 7). When normalized to the average composition of the Hrepphólar lava, the trace elements display nearly identical trends (only shifted above or below the average), whereas the REE show sometimes opposite trends (Fig. 7). There are, however, slight but significant Eu-anomalies (both positive and negative) within the column. This is even more evident when normalized against the average composition (with Europium anomalies ranging from 0.913 to 1.092 relative to the average of all 27 samples), reflecting the variable plagioclase content across the column.

### Mineral chemistry

The most abundant phenocrysts, plagioclase, display normal zoning characterized by decreasing anorthite content towards the rim (Table 2a). The plagioclase core compositions vary between  $\text{An}_{90}$  and  $\text{An}_{65}$ , with slightly more evolved outer rims ranging between  $\text{An}_{82}$  and  $\text{An}_{34}$ . Also the smaller crystals (microphenocrysts) display considerable compositional variation ranging from  $\text{An}_{98}$  to  $\text{An}_{53}$ . In general, the An content varies more in phenocrysts than in microphenocrysts. Across the whole column, there is no clear systematic trend between phenocryst core/rim-compositions at the edge of the column with the same compositions in the center of it (Table 2a). The composition of the microphenocrysts differs slightly from the composition of the phenocrysts, with the former having slightly higher  $\text{SiO}_2$  and CaO contents compared with the latter.

The most variable oxide in the clinopyroxenes is FeO, with rims more enriched in FeO than the cores of single grains (i.e., normal zonation; Table 2b). The clinopyroxene core compositions range from  $\text{En}_{48}\text{Fs}_{14}\text{Wo}_{38}$  to  $\text{En}_{44}\text{Fs}_{15}\text{Wo}_{41}$ , whereas the rims vary between  $\text{En}_{46}\text{Fs}_{20}\text{Wo}_{34}$  and  $\text{En}_{42}\text{Fs}_{20}\text{Wo}_{38}$  (Table 2b).



**Table 1** Major- and trace element analyses from profile A through the basalt column

Sample	A1	A2	A3	A4	A5	A6	A7	A8	A9	A10	A11	A12	A13
SiO <sub>2</sub>	49.17	48.93	48.94	49.01	49.01	48.87	49.00	49.14	48.58	49.15	49.32	49.41	49.23
TiO <sub>2</sub>	2.71	2.72	2.72	2.85	2.83	2.83	2.80	2.80	2.74	2.74	2.70	2.70	2.69
Al <sub>2</sub> O <sub>3</sub>	13.21	13.18	13.18	12.97	13.01	13.06	13.05	12.99	12.95	13.14	13.31	13.10	13.21
Fe <sub>2</sub> O <sub>3</sub> <sup>T</sup>	15.21	15.42	15.31	15.69	15.43	15.80	15.62	15.62	15.16	15.33	15.16	15.14	15.14
MnO	0.23	0.23	0.23	0.23	0.23	0.23	0.23	0.23	0.23	0.23	0.23	0.23	0.23
MgO	6.21	6.31	6.25	6.12	5.89	6.17	6.11	6.13	6.03	6.15	6.13	6.22	6.20
CaO	10.80	10.72	10.77	10.65	10.49	10.76	10.60	10.51	10.48	10.63	10.69	10.71	10.71
Na <sub>2</sub> O	2.41	2.43	2.45	2.42	2.48	2.42	2.42	2.42	2.42	2.41	2.43	2.40	2.45
K <sub>2</sub> O	0.42	0.41	0.41	0.43	0.46	0.42	0.43	0.44	0.42	0.42	0.42	0.42	0.43
P <sub>2</sub> O <sub>5</sub>	0.28	0.28	0.28	0.31	0.33	0.30	0.31	0.32	0.31	0.30	0.30	0.30	0.30
Total	100.63	100.63	100.54	100.70	100.15	100.86	100.57	100.59	99.30	100.50	100.69	100.65	100.58
Mg#	26.26	26.28	26.26	25.38	24.97	25.39	25.42	25.48	25.74	25.91	26.06	26.38	26.31
Rb	7.45	6.99	6.99	7.83	7.91	7.44	7.53	7.60	7.74	7.05	6.68	6.17	6.10
Sr	205	204	207	208	203	202	207	205	207	205	199	192	189
Zr	152	154	153	156	178	157	169	174	167	160	176	169	174
Nb	18.7	19.0	18.9	21.3	21.8	18.9	20.8	20.9	21.0	20.5	19.6	19.3	18.3
Mo	1.35	1.87	2.32	1.55	1.71	2.84	2.49	2.36	2.49	2.45	2.18	2.04	1.96
Cs	0.09	0.08	0.10	0.09	0.10	0.11	0.10	0.11	0.09	0.10	0.09	0.07	0.07
Ba	93.3	92.9	93.0	101.6	104.7	94.8	101.0	100.4	97.1	94.2	87.5	85.8	85.3
La	14.5	14.8	14.7	15.8	16.9	15.4	16.6	16.6	15.6	15.1	15.4	15.2	15.5
Ce	33.9	34.7	34.6	38.7	40.2	35.9	38.4	38.5	36.3	34.8	31.9	32.3	30.5
Pr	4.46	4.70	4.63	5.12	5.42	4.82	5.25	5.11	4.74	4.61	4.52	4.47	4.42
Nd	21.3	21.9	21.9	23.3	25.1	22.4	24.5	24.3	22.5	21.8	22.8	22.1	21.8
Sm	5.79	5.71	5.68	5.96	6.46	5.69	6.46	6.18	5.85	5.68	5.77	5.92	5.92
Eu	1.85	1.92	1.92	2.01	2.09	1.94	2.01	2.00	1.87	1.85	1.85	1.78	1.87
Gd	6.17	6.38	6.32	6.16	7.10	6.57	6.94	6.90	6.17	6.24	6.43	6.91	7.14
Tb	0.99	1.00	1.01	0.97	1.15	1.06	1.09	1.06	0.95	0.92	1.06	1.02	1.06
Dy	6.15	6.31	6.45	6.23	7.17	6.29	6.71	6.95	5.89	5.83	6.61	6.49	6.71
Ho	1.26	1.23	1.24	1.27	1.46	1.34	1.38	1.40	1.17	1.21	1.33	1.29	1.37
Er	3.53	3.58	3.47	3.51	4.15	3.83	3.94	3.90	3.54	3.53	3.92	3.59	3.90
Tm	0.47	0.49	0.48	0.48	0.56	0.53	0.52	0.55	0.43	0.45	0.51	0.45	0.51
Yb	2.99	3.17	3.15	3.06	3.49	3.29	3.43	3.63	3.09	3.10	3.44	3.58	3.58
Lu	0.45	0.49	0.49	0.47	0.56	0.48	0.53	0.53	0.45	0.47	0.50	0.47	0.54
Hf	4.02	4.21	4.20	4.13	4.89	4.20	4.54	4.72	3.94	4.00	4.43	4.13	4.48
Ta	1.22	1.24	1.19	1.33	1.41	1.23	1.39	1.42	1.29	1.25	1.31	1.27	1.25
W	0.18	0.25	0.11	0.19	0.21	0.16	0.16	0.14	0.13	0.06	0.09	0.24	0.26
Th	1.31	1.32	1.30	1.38	1.52	1.40	1.43	1.47	1.46	1.42	1.48	1.37	1.39
U	0.41	0.39	0.40	0.44	0.47	0.43	0.45	0.45	0.43	0.40	0.35	0.39	0.35

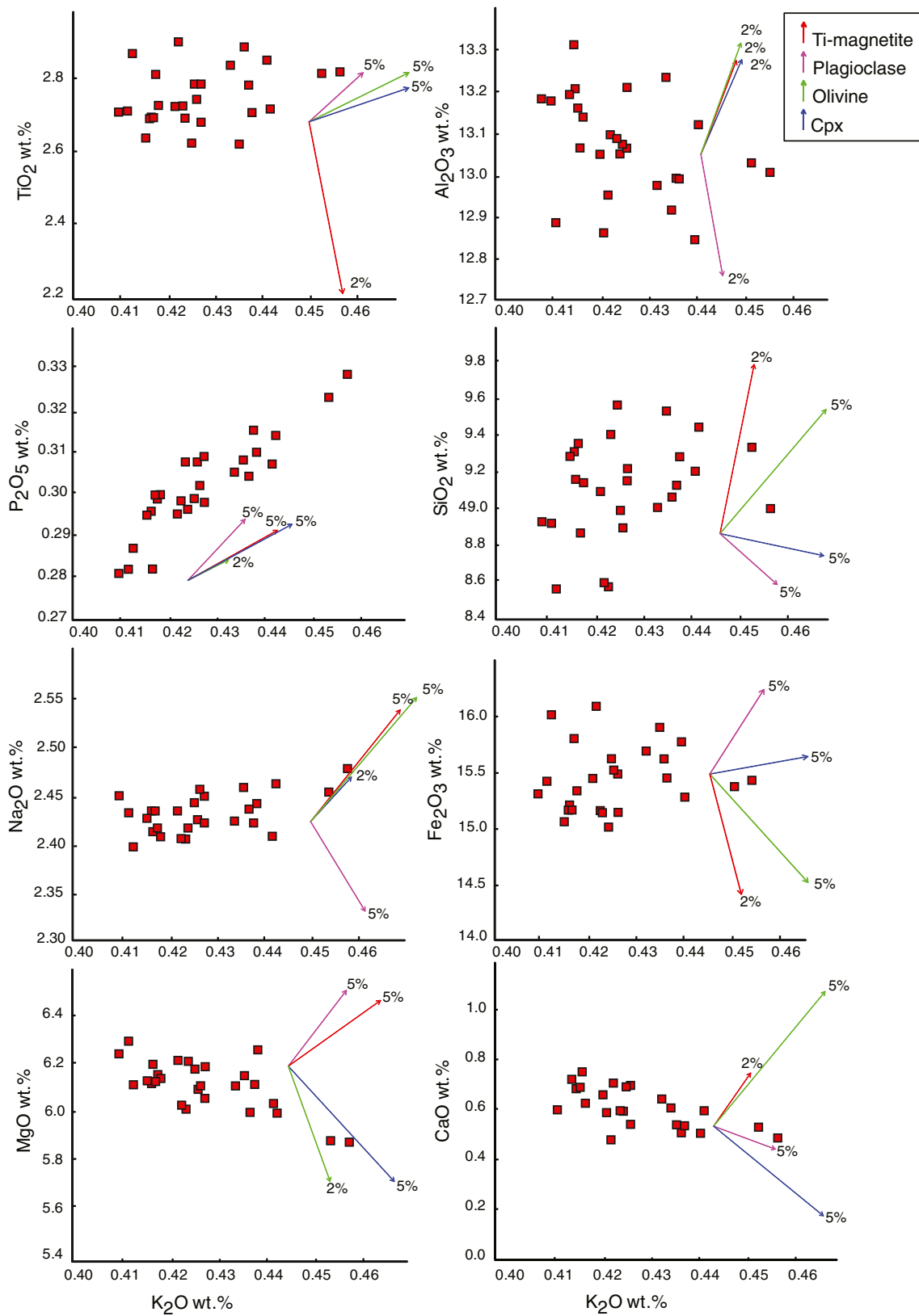
  

Sample	A14	A15	A16	A17	A18	A19	A20	A21	A22	A23	A24	A25	A26	A27
SiO <sub>2</sub>	49.16	49.36	49.29	49.10	49.45	49.29	48.90	49.54	49.57	48.57	48.60	49.07	49.21	49.34
TiO <sub>2</sub>	2.80	2.71	2.65	2.74	2.73	2.72	2.76	2.63	2.64	2.88	2.92	2.90	2.87	2.83
Al <sub>2</sub> O <sub>3</sub>	13.06	13.16	13.19	13.05	13.12	12.99	13.07	13.23	13.09	12.89	12.86	12.92	12.84	13.03
Fe <sub>2</sub> O <sub>3</sub> <sup>T</sup>	15.48	15.16	15.06	15.44	15.28	15.45	15.52	15.10	15.01	16.01	16.09	15.90	15.77	15.37

Table 1 (continued)

Sample	A14	A15	A16	A17	A18	A19	A20	A21	A22	A23	A24	A25	A26	A27
MnO	0.23	0.23	0.23	0.23	0.23	0.23	0.23	0.23	0.23	0.23	0.23	0.23	0.23	0.23
MgO	6.07	6.14	6.14	6.23	6.01	6.27	6.12	6.16	6.19	6.13	6.04	6.01	6.05	5.90
CaO	10.55	10.70	10.73	10.67	10.60	10.54	10.70	10.61	10.60	10.61	10.59	10.55	10.51	10.54
Na <sub>2</sub> O	2.42	2.43	2.43	2.43	2.46	2.44	2.46	2.46	2.44	2.40	2.40	2.43	2.41	2.45
K <sub>2</sub> O	0.43	0.42	0.42	0.42	0.44	0.44	0.43	0.44	0.43	0.41	0.42	0.44	0.44	0.45
P <sub>2</sub> O <sub>5</sub>	0.31	0.30	0.30	0.30	0.31	0.31	0.30	0.31	0.30	0.29	0.30	0.30	0.31	0.32
Total	100.51	100.61	100.43	100.61	100.64	100.68	100.49	100.7	100.5	100.4	100.5	100.8	100.6	100.5
Mg#	25.47	26.09	26.23	26.01	25.53	26.14	25.59	26.24	26.45	25.01	24.67	24.79	25.06	25.06
Rb	7.99	6.75	6.30	6.31	7.79	7.50	6.98	7.44	7.25	6.80	7.03	7.11	7.40	7.48
Sr	197	194	191	189	205	203	198	211	211	204	203	200	201	200
Zr	153	155	167	167	155	155	166	181	178	174	170	172	175	174
Nb	21.1	19.8	18.6	18.6	21.5	21.4	19.3	18.8	18.2	17.3	17.6	17.4	18.0	18.2
Mo	3.09	2.38	2.49	2.22	3.07	3.44	2.28	3.13	3.23	3.64	2.74	2.74	3.23	2.14
Cs	0.12	0.08	0.06	0.07	0.07	0.07	0.07	0.07	0.08	0.07	0.06	0.06	0.06	0.07
Ba	96.4	90.4	86.2	89.3	102.0	100.4	93.0	96.4	95.6	92.9	95.7	97.2	97.7	100.5
La	15.3	14.9	14.9	15.1	15.9	15.4	15.5	16.3	16.1	15.8	15.8	16.0	16.4	16.9
Ce	35.0	32.9	31.6	31.6	37.7	37.1	34.8	36.7	35.7	34.5	35.5	35.8	36.6	37.9
Pr	4.80	4.69	4.58	4.51	5.01	4.97	4.67	4.89	4.75	4.68	4.75	4.83	4.86	5.15
Nd	22.3	22.4	21.7	22.9	23.0	23.4	23.1	23.4	23.4	22.8	22.9	22.9	23.8	23.7
Sm	5.82	5.97	5.73	5.46	5.91	5.51	5.99	6.11	6.23	5.82	5.84	6.02	6.18	6.44
Eu	1.89	1.87	1.76	2.05	1.89	1.85	1.92	1.86	1.83	1.82	1.97	1.88	1.97	2.04
Gd	5.85	6.35	6.68	7.32	6.13	6.58	6.59	6.22	6.77	6.86	6.88	7.09	6.71	7.22
Tb	0.94	0.93	0.99	0.97	1.01	0.92	1.02	1.09	1.07	1.04	1.04	1.00	1.05	1.07
Dy	6.02	6.00	6.69	6.48	6.06	6.04	6.69	6.56	6.69	6.71	6.86	6.75	7.32	6.88
Ho	1.14	1.17	1.34	1.30	1.18	1.22	1.29	1.35	1.33	1.39	1.31	1.32	1.30	1.36
Er	3.37	3.53	3.86	4.05	3.53	3.58	3.97	4.24	3.85	3.95	3.75	3.71	3.85	4.06
Tm	0.47	0.41	0.52	0.55	0.51	0.46	0.48	0.49	0.50	0.54	0.55	0.51	0.53	0.52
Yb	3.24	2.95	3.24	3.32	3.29	3.05	3.50	3.29	3.60	3.43	3.64	3.41	3.50	3.73
Lu	0.43	0.49	0.51	0.45	0.49	0.45	0.46	0.54	0.55	0.54	0.51	0.54	0.53	0.54
Hf	3.86	3.88	4.21	4.43	4.11	4.12	4.23	4.49	4.54	4.50	4.62	4.46	4.74	4.64
Ta	1.37	1.25	1.31	1.19	1.26	1.31	1.23	1.27	1.18	1.18	1.17	1.17	1.23	1.17
W	0.16	0.20	0.17	0.15	0.54	0.20	0.20	0.12	0.13	0.11	0.14	0.11	0.12	0.12
Th	1.28	1.29	1.36	1.40	1.41	1.36	1.40	1.51	1.57	1.53	1.49	1.47	1.43	1.49
U	0.39	0.35	0.35	0.41	0.41	0.43	0.37	0.42	0.43	0.41	0.42	0.45	0.41	0.37

Mg# = 100\*(Mg/(Mg+Fe<sup>2+</sup>)), Fe<sup>2+</sup> = 0.89\*Fe<sub>2</sub>O<sub>3</sub><sup>T</sup> (Gill 2010). All Fe reported as Fe<sub>2</sub>O<sub>3</sub><sup>T</sup>



**Fig. 5** Major element variation diagrams of the samples from the A-profile (Fig. 3). The red squares correspond to samples and the arrows indicate the direction of the evolving melt, if crystallizing 2 or 5 % of

plagioclase (pink), titanomagnetite (red), clinopyroxene (blue), or olivine (green). The length of the arrow corresponds directly to the amount (marked in percent) of the crystallizing mineral



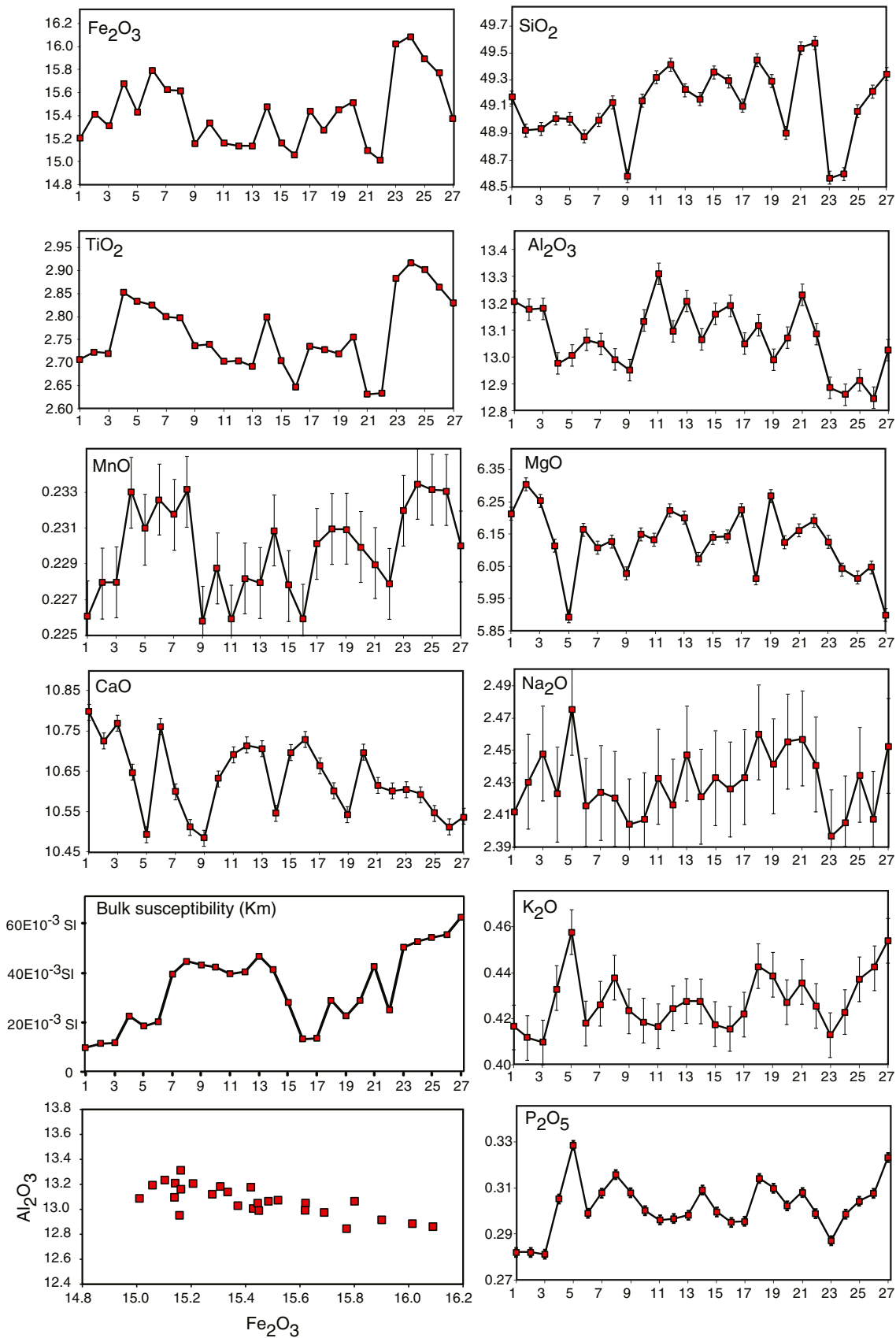


**Fig. 6** Variation of the major elements (in weight percent) and the bulk susceptibility ( $K_m$ , in SI) from AMS measurements as a function of their location within the A-profile (A1–A27) across the column. Error bars indicate  $2\sigma$  statistical error of the analyses. Some correlation can be seen between certain elements (i.e.,  $TiO_2$ ,  $Fe_2O_3$ ,  $SiO_2$ , and  $Al_2O_3$ ) and the structures inside the column (e.g., high  $TiO_2$  and  $Fe_2O_3$  where the dark bands are visible and thus low  $SiO_2$  and  $Al_2O_3$ ). A negative correlation can be seen when plotting  $Al_2O_3$  vs. FeO

All compositional analyses of olivine report core compositions (Table 2c), as only one of the analyzed olivine crystals showed zoning. In general, the composition of the olivines ranges from  $Fo_{52}$  to  $Fo_{41}$  in the different samples. The reversed zoning found in one of the olivines is considerable, ranging from  $Fo_{35}$  in the core to  $Fo_{48}$  at the rim, and it is interpreted as a xenocryst due to the very low Fo core. Olivine is absent as a groundmass mineral.

Opaque minerals are titanomagnetite and ilmenite. Typically the titanomagnetites range in composition between  $Mag_{32}Usp_{68}$  and  $Mag_{18}Usp_{82}$  in the phenocrysts and  $Mag_{38}Usp_{62}$  and  $Mag_{15}Usp_{85}$  in the microphenocrysts (Table 2d). The ilmenites vary only slightly in composition between  $Ilm_{97}Hem_3$  and  $Ilm_{93}Hem_7$  (Table 2e). Applying the geothermometer based on coexisting titanomagnetite–ilmenite pairs (Sauerzapf et al. 2008) yields crystallization temperatures of  $994 \pm 6$  °C. There is no noticeable difference in temperatures calculated for titanomagnetite–ilmenite pairs in the brighter- vs. darker-colored bands.

## 2D-orientation and CSD of plagioclase

The 2D-orientations (inclinations) in the vertical plane of plagioclase laths were measured from photographs of thin sections (Fig. 8). The thin sections were cut from the lower part of the plane so that the plane of the sections is parallel to the plane of the plate (Fig. 3a). Inclinations of plagioclase crystals were measured between  $0^\circ$  and  $180^\circ$ , with  $90^\circ$  being vertical, and mirrored in the rose diagrams to accentuate the measured orientations. Although the exact orientation of the c-axes in the crystals is not known, the elongate lath shape of plagioclase crystals allows intersection trends to be used as a rough indicator of orientation (Smith 2002 and references therein). The plagioclase data were divided into two groups with a limit set at 0.2 mm in order to differentiate between the macrophenocrysts ( $>0.2$  mm) and microphenocrysts ( $\leq 0.2$  mm). The measured orientation is similar for most crystals, and no clear difference can be seen between orientations of macrophenocrysts versus microphenocrysts. Most crystal orientations plot in the upper right quadrant of the diagram. Some samples (e.g., the macrophenocrysts in LS4 and LS7) stand out from this general orientation as these are oriented near-parallel to the long axis of the column (Fig. 8).

Stereologically corrected crystal size distribution data (Table 3) was plotted on a classic CSD diagram of ln

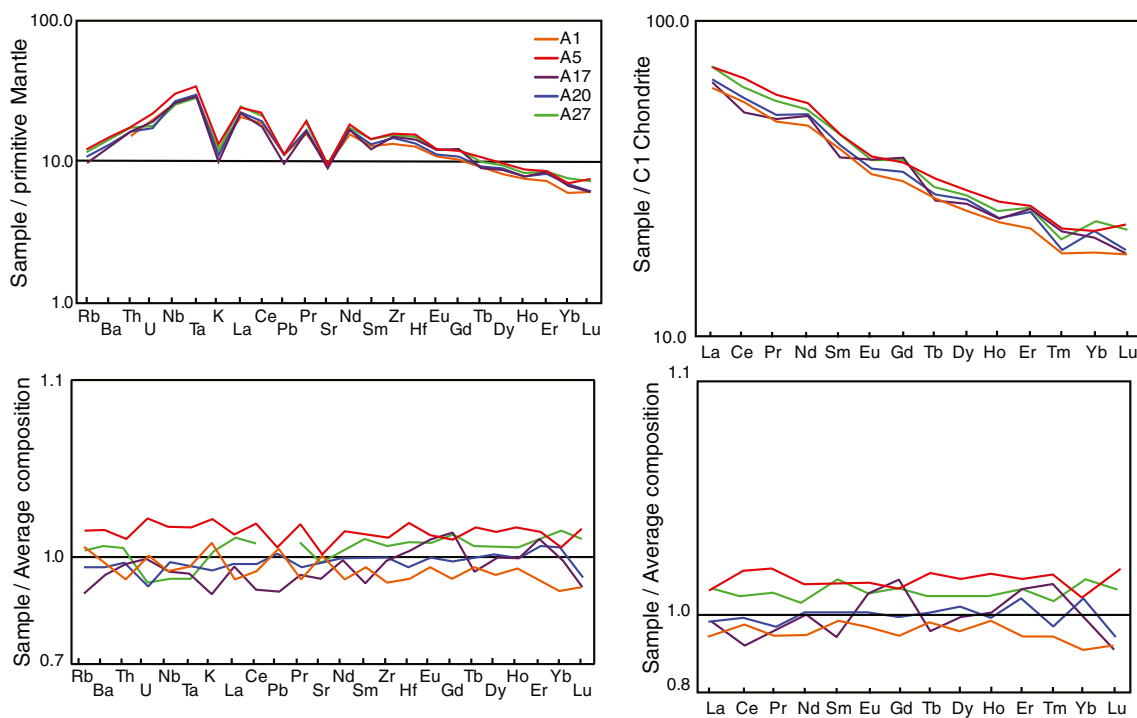


**Fig. 7** REE and trace element diagrams of selected samples. REE were normalized to C1 chondrite, trace elements to primitive mantle values after Sun and McDonough (1989). *Left* trace elements normalized to the primitive mantle (*top left*) and to the total average

composition of all 27 samples (*lower left*). *Right* REE normalized to the C1-chondrite (*top right*) and to the total average composition of all 27 samples (*lower right*). In both these diagrams, the element Pb is missing in sample A27, as this value was below the detection limit

**Table 2** Representative microprobe analyses of phenocryst phases in the Hrepphólar basalt column

Sample	Location	SiO <sub>2</sub>	Na <sub>2</sub> O	CaO	K <sub>2</sub> O	FeO <sup>T</sup>	Al <sub>2</sub> O <sub>3</sub>	MgO	P <sub>2</sub> O <sub>5</sub>	TiO <sub>2</sub>	Cr <sub>2</sub> O <sub>3</sub>	Total
(a) Plagioclase												
LS1	Core	51.04	3.19	14.33	0.10	0.90	29.31	0.152	0.014	0.098	–	99.14
	Rim	53.9	4.73	12.24	0.19	0.85	27.26	0.156	–	0.090	–	99.42
	Micro	52.47	3.87	13.35	0.13	1.04	28.36	0.088	0.022	0.098	0.026	99.46
LS2	Core	52.57	3.57	13.67	0.13	0.82	29	0.154	0.038	0.085	–	100.03
	Rim	56.86	5.49	10	0.33	1.30	25.55	0.170	0.051	0.206	0.040	99.99
	Micro	52.97	3.79	13.11	0.16	1.55	28.09	0.163	0.054	0.122	–	100.00
LS3	Core	51.45	3.36	14.16	0.12	0.91	29.23	0.116	–	0.066	0.004	99.42
	Rim	54.29	4.46	12.09	0.19	1.06	27.38	0.114	–	0.145	–	99.73
	Micro	53.29	3.85	13.04	0.13	1.10	28.48	0.121	0.018	0.110	0.025	100.17
LS4	Core	54.44	4.38	12.12	0.20	0.85	27.37	0.132	0.012	0.122	–	99.63
	Rim	55.99	5.21	10.78	0.25	1.06	26.27	0.097	–	0.173	0.010	99.84
	Micro	55.7	5	11.11	0.26	1.10	26.29	0.114	0.004	0.200	–	99.78
LS5	Core	48.75	2.84	13.18	0.16	8.12	23.61	1.850	0.120	1.360	0.001	100.00
	Rim	54.62	4.29	12.34	0.22	0.97	27.63	0.107	–	0.139	0.001	100.31
	Micro	54.51	4.58	11.83	0.21	1.07	26.85	0.121	0.034	0.119	–	99.32
LS6	Core	52.14	3.91	13.86	0.11	0.79	28.58	0.209	0.031	0.072	0.015	99.72
	Rim	55.18	4.7	11.68	0.21	0.79	27.04	0.102	–	0.095	0.026	99.82
	Micro	54.53	4.5	12	0.20	1.02	27.38	0.104	0.021	0.141	–	99.90
LS7	Core	51.84	3.38	14.44	0.12	0.73	29.18	0.142	0.012	0.104	0.001	99.94
	Rim	56.04	5.11	10.82	0.24	0.85	26.69	0.087	–	0.149	0.011	100.00
	Micro	56.36	5.04	10.81	0.24	0.92	26.46	0.151	0.014	0.143	0.017	100.15
LS	Core	51.49	3.3	14.23	0.10	0.88	29.4	0.155	0.031	0.090	–	99.67
	Rim	54.55	4.45	12.23	0.20	0.78	27.93	0.106	0.029	0.112	0.006	100.40
	Micro	52.85	3.59	13.31	0.14	1.01	29.06	0.145	0.037	0.085	0.009	100.24
LS9	Core	49.88	2.55	15.94	0.07	0.85	30.67	0.089	–	0.080	0.024	100.15
	Rim	54.89	4.46	11.98	0.18	0.86	27.42	0.141	0.012	0.100	–	100.05
	Micro	55.23	4.76	11.98	0.19	1.16	26.64	0.133	0.014	0.093	0.007	100.21
LS10	Core	52.92	3.6	13.44	0.13	0.88	27.84	0.150	0.000	0.104	–	99.07
	Rim	56.47	5.2	10.45	0.29	1.28	25.18	0.274	0.035	0.136	–	99.32
	Micro	54.64	4.36	12.39	0.17	0.92	27.12	0.106	0.011	0.120	0.026	99.86
(b) Clinopyroxene												
LS1	Core	50.26	0.316	19.34	–	8.93	4.00	15.74	0.006	1.22	0.281	100.10
	Rim	51.29	0.130	16.23	–	13.68	1.63	16.06	0.027	0.95	0.007	100.00
LS2	Core	50.62	0.322	18.78	–	12.20	2.63	14.54	0.012	1.38	0.022	100.51
	Rim	50.35	0.246	18.76	0.02	10.39	3.57	15.38	–	1.40	0.037	100.15
LS3	Rim	51.21	0.228	17.79	0.01	12.68	1.79	15.11	0.056	1.01	–	99.89
	Core	50.79	0.296	20.25	–	8.90	3.12	15.59	–	0.99	0.207	100.15
LS4	Core	52.04	0.213	20.13	–	8.20	2.02	16.14	–	0.68	0.183	99.61
	Rim	51.61	0.261	18.18	–	12.52	1.62	15.26	–	1.00	0.030	100.48
LS5	Core	51.76	0.192	15.62	0.01	15.06	1.19	15.35	–	0.90	0.001	100.09
	Rim	51.76	0.218	15.90	–	13.67	1.32	16.21	–	0.81	0.006	99.90
LS6	Core	51.25	0.241	20.04	0.02	8.90	3.02	15.66	–	1.00	0.143	100.27
	Rim	51.15	0.306	18.16	–	12.29	2.16	14.85	0.059	1.12	0.021	100.12
LS7	Core	50.14	0.337	19.15	0.01	11.43	3.70	14.4	0.038	1.38	0.067	100.65
	Rim	51.83	0.303	18.17	0.05	12.63	1.91	14.51	0.015	1.03	–	100.45
LS	Core	49.61	0.334	19.88	–	9.43	4.13	15.01	0.020	1.57	0.102	100.08
	Rim	51.80	0.192	17.54	–	12.55	1.66	14.97	0.033	0.99	0.021	99.76
LS9	Core	51.29	0.244	20.69	0.01	8.26	2.98	15.67	–	0.95	0.222	100.31



**Table 2** (continued)

Sample	Location	SiO <sub>2</sub>	Na <sub>2</sub> O	CaO	K <sub>2</sub> O	FeO <sup>T</sup>	Al <sub>2</sub> O <sub>3</sub>	MgO	P <sub>2</sub> O <sub>5</sub>	TiO <sub>2</sub>	Cr <sub>2</sub> O <sub>3</sub>	Total
LS10	Rim	50.81	0.235	15.80	0.01	18.92	1.41	12.17	0.012	1.04	0.003	100.41
	Core	53.12	0.193	18.73	–	8.60	1.93	17.08	0.005	0.70	0.161	100.52
	Rim	52.26	0.225	18.05	0.01	12.70	1.63	15.22	0.006	1.03	0.009	101.14
(c) Olivine												
LS1	Core	36.93	0.049	0.2772	0.01	31.49	–	31.99	0.074	0.04	–	100.86
LS2	Core	36.84	–	0.2838	0.01	33.17	0.0006	31.11	0.088	0.04	0.003	101.54
LS3	Core	36.21	–	0.2734	–	37.25	–	27.68	0.004	0.04	0.002	101.46
LS4	Core	37.56	–	0.2613	0.01	31.41	–	32.12	–	0.03	0.015	101.41
LS5	Core	37.05	0.002	0.2933	–	33.01	0.0097	30.86	0.043	0.04	–	101.30
	Rim	35.51	–	0.3343	0.0045	42.33	–	23.64	0.0404	0.0166	0.0207	101.90
LS6	Core	36.07	0.025	0.3551	0.00	33.58	0.0484	29.17	0.038	0.05	–	99.34
LS7	Core	37.73	0.060	0.3295	0.01	33.59	0.035	29.62	0.084	0.01	0.037	101.51
LS	Core	36.70	–	0.3044	0.01	34.88	0.0637	19.44	0.043	0.02	–	101.46
LS9	Core	36.92	0.022	0.3282	0.01	34.23	–	29.63	0.033	0.02	0.006	101.20
LS10	Core	36.54	0.077	0.3027	0.00	37.84	–	27.18	0.031	0.03	–	102.00
(d) Titanomagnetite												
LS1	Pheno	0.05	–	0.042	–	69.26	1.68	0.872	0.005	25.57	0.023	97.50
	Micro	0.03	0.019	0.169	–	68.34	1.90	1.122	–	25.24	0.026	96.84
LS2	Pheno	0.10	0.130	0.079	0.00	68.7	1.84	0.931	–	25.57	0.025	97.37
	Micro	0.07	–	0.293	0.01	67.51	1.95	1.780	–	24.70	0.048	96.36
LS3	Pheno	0.06	–	0.058	0.01	69.4	2.04	0.816	–	25.01	0.055	97.45
	Micro	0.39	0.059	0.122	0.06	72.1	1.69	0.210	–	21.04	0.032	95.70
LS4	Pheno	0.11	0.015	0.007	0.00	69.83	2.38	1.369	–	23.41	0.168	97.29
	Micro	0.04	–	0.059	0.01	70.65	1.93	0.620	0.020	23.89	0.034	97.25
LS5	Pheno	–	–	0.015	–	69.48	2.37	1.568	0.021	23.53	0.196	97.18
	Micro	0.05	0.015	0.087	0.00	71.52	1.56	0.246	0.027	23.29	–	96.80
LS6	Pheno	0.05	0.026	0.021	0.02	70.52	2.14	1.059	–	23.61	0.069	97.51
	Micro	–	0.1262	0.1244	0.0084	68.46	1.8431	0.5948	–	24.3	–	95.457
LS7	Pheno	0.11	–	0.023	–	69.73	2.16	1.299	–	24.06	0.102	97.49
	Micro	0.0718	0.0496	0.0914	0.0205	69.23	1.7824	0.6247	–	24.52	0.0084	96.3989
LS	Pheno	0.04	–	0.018	0.01	69.26	1.89	1.070	0.004	24.98	0.080	97.35
	Micro	0.05	–	0.029	–	68.76	1.81	0.971	–	25.37	0.038	97.02
LS9	Pheno	0.05	0.102	0.029	–	69.68	1.91	0.923	–	24.66	0.011	97.37
	Micro	–	–	0.147	0.02	68.23	1.59	0.985	–	25.79	0.053	96.81
LS10	Pheno	0.06	–	0.051	–	68.78	1.53	0.700	–	25.99	0.014	97.12
	Micro	0.0062	–	0.2306	–	69.05	1.6902	0.6295	0.0093	24.48	0.0302	96.1261
(e) Ilmenite												
LS4	Pheno	–	–	0.272	0.0212	48.5	0.12	0.968	–	49.39	0.004	99.03
	Micro	–	–	0.3261	0.0047	47.87	0.1932	0.9267	0.0167	48.86	0.0171	98.2145
LS5	Micro	0.7006	0.0981	0.258	0.0076	46.7	0.2431	0.9038	0.02	47.62	0.0122	96.5634
LS6	Micro	–	0.027	0.1579	–	48.49	0.0634	0.641	0.0012	49.24	0.0353	98.6558
LS7	Micro	–	0.0622	0.2248	0.0144	47.3	0.0793	0.7738	–	49.91	–	98.3645
LS10	Micro	0.0267	–	0.0796	0.0037	47.48	0.1274	0.8652	0.0422	49.98	0.0304	98.6352

(population density) versus crystal size (Fig. 9a). A representative example of a digitized thin section used for the CSD analysis is presented in Fig. 9b. All samples show similar trends in the CSD plots, with samples LS2, LS3,

LS5, and LS8 containing the largest plagioclase crystals (>1.6 mm; Fig. 9a). The total amount of plagioclase in the different thin sections varies between 50.9 (LS6) and 64.3 vol.% (LS5). The intercepts of the CSDs range from

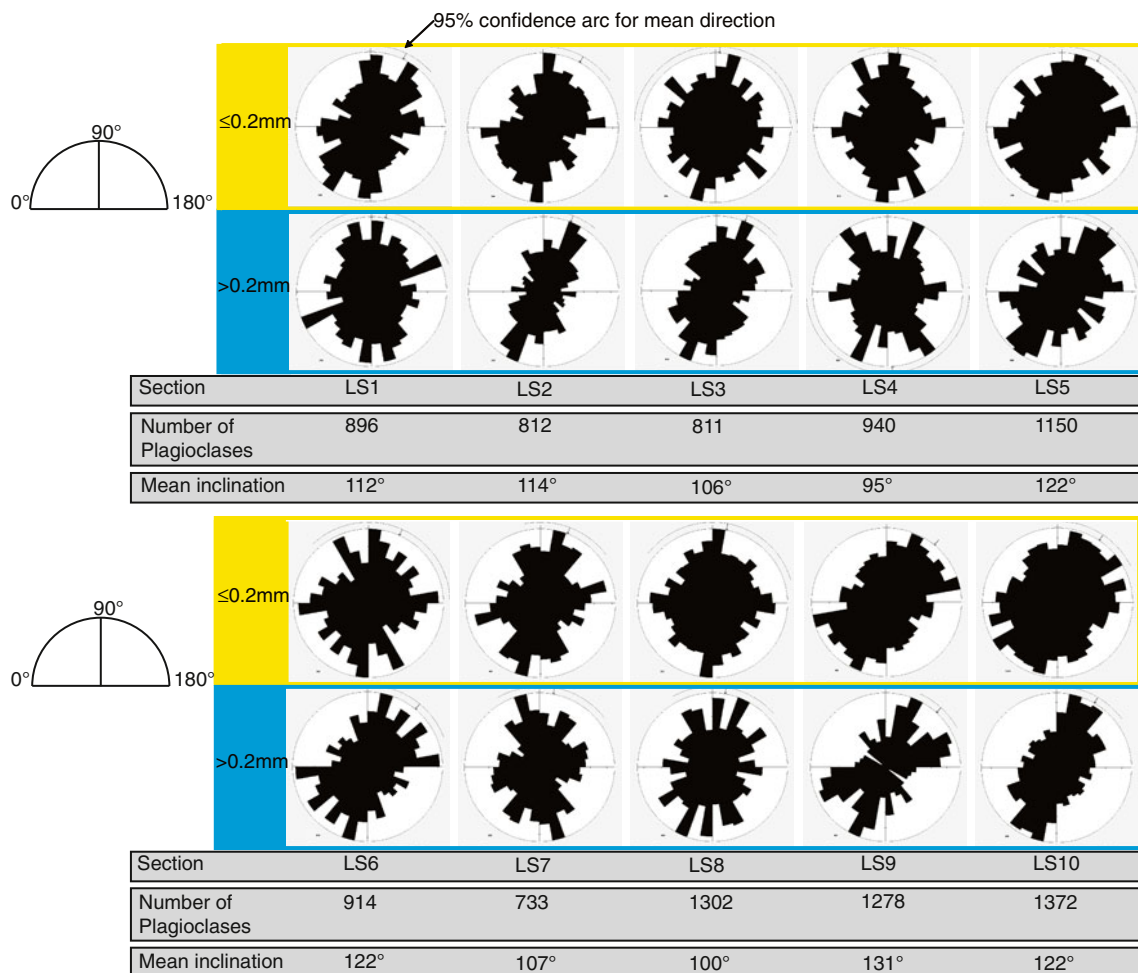


**Fig. 8** Rose diagram showing the orientation of plagioclase macrophenocrysts ( $>2$  mm) and microphenocrysts ( $\leq 2$  mm) along the profile (i.e., LS1 to LS10). The mean direction is clockwise with respect to the

column's long axis. There is no clear difference between the orientations of the macrophenocrysts and the microphenocrysts, but the majority of the crystal orientations plot in the first quadrant of the diagram

7.07 (LS4) to 7.96 (LS9), and the slope of the regression line from  $-5.04$  (LS7) to  $-7.8$  (LS9). By plotting the slopes of the regression lines for the CSDs against location within the polished slab, we show that samples from the sides of the columns have steeper slopes in the CSD's, followed by a flattening trend inwards (Fig. 9c). However, there is a region near the center of the slab where the CSDs steepen again (samples LS5 and LS6; Fig. 9c). The crystal number density (CND) of plagioclase shows that there are more crystals near the center of the column and at the edges of the plate than in the areas in between (Fig. 9c). In general, the slope of the CSD and the CND of the samples show an inverse correlation (i.e., the higher the CND the steeper the CSD slope). In addition to this, there is also a rough correlation between observed 2D-trends of plagioclase laths and the slope of the CSD plot (Fig. 9d). In general, steeper CSD slopes are associated with more subhorizontally oriented crystals whereas flatter CSD's are coupled to more steeply inclined plagioclase laths.

## Discussion

### Geochemistry and mineral chemistry

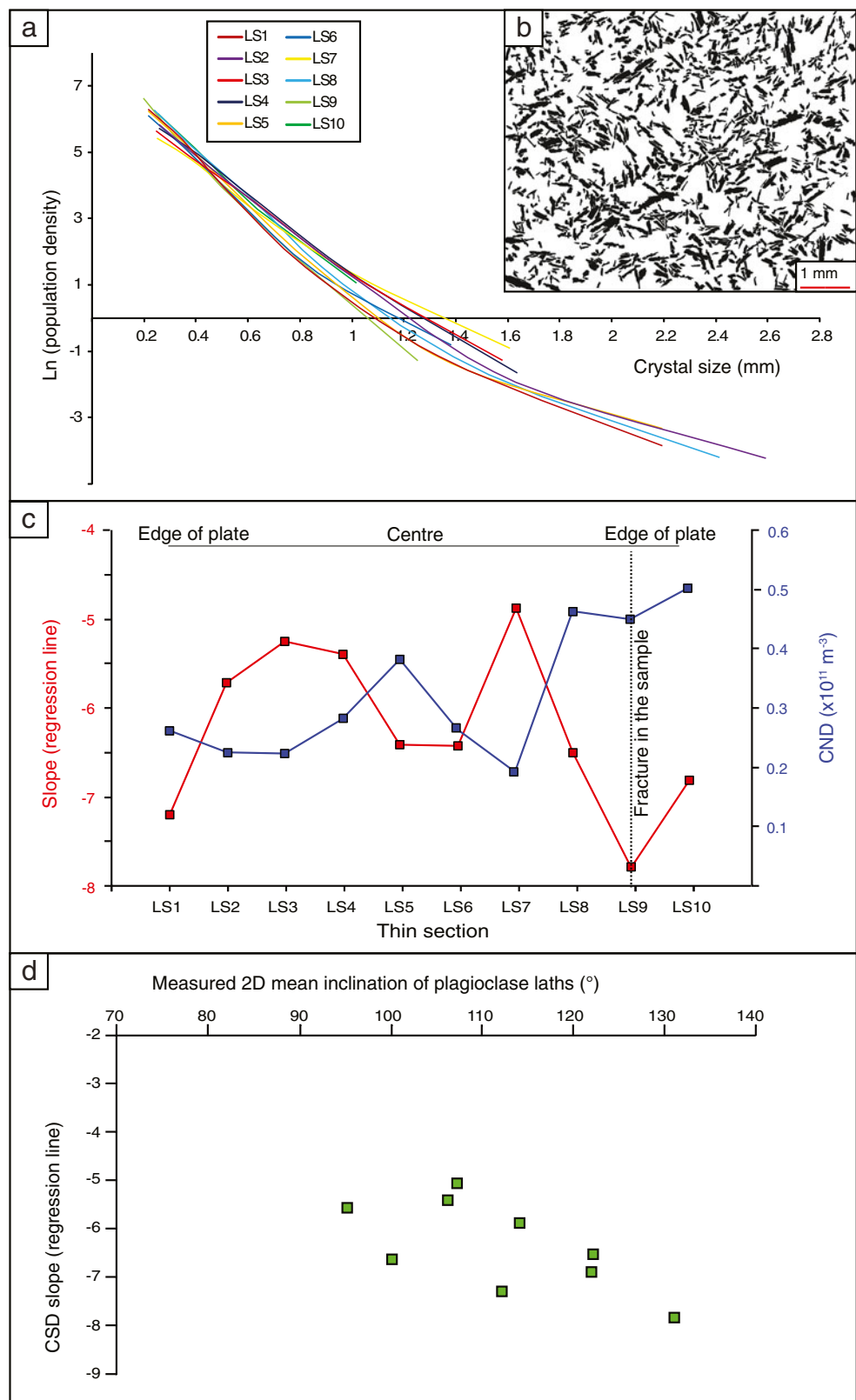
It is clear from petrography that the alternating brighter and darker bands inside the columns reflect variations in the modal proportions of the main crystallizing phases (i.e., plagioclase, clinopyroxene, and titanomagnetite/ilmenite), where the dark bands contain 7 modal% titanomagnetite and the bright bands 4 modal% titanomagnetite. In a typical low pressure crystallization sequence for basaltic compositions, olivine and plagioclase crystals are first on the solidus followed by clinopyroxene (Wright and Okamura 1977; Philpotts and Dickson 2002). Crystallizing plagioclase and olivine depletes melt in elements like Na, Mg, Ca, and Al, while enriching it in elements like Fe and Ti (Philpotts and Dickson 2002). This change in chemistry finally stabilizes titanomagnetite and ilmenite in the end of the crystallization sequence. Similar modal layering has been reported from

**Table 3** Results of CSD analyses of plagioclase in the Hrepphólar basalt column

Sample	LS2		LS3		LS4		LS5		LS6		LS7		LS8		LS9		LS10		
	Size	PD	Size	PD	Size	PD	Size	PD	Size	PD	Size	PD	Size	PD	Size	PD	Size	PD	
	2.190	-3.849	2.587	-4.212	-	-	-	-	2.190	-3.337	-	-	-	-	2.409	-4.191	-	-	-
	1.382	-1.345	1.632	-1.932	1.574	-1.265	1.632	-1.626	1.382	-1.358	1.377	-0.791	1.603	-0.914	1.520	-1.684	1.25	-1.298	-
	0.872	1.223	1.030	1.080	0.993	1.316	1.030	1.175	0.872	1.454	0.869	1.346	1.011	1.299	0.959	1.064	0.79	1.782	1.011
	0.550	3.580	0.650	3.315	0.627	3.505	0.650	3.422	0.550	3.795	0.548	3.646	0.638	3.183	0.605	3.667	0.5	3.943	0.638
	0.347	5.372	0.410	4.827	0.395	4.761	0.410	4.912	0.347	5.316	0.346	5.191	0.403	4.672	0.382	5.193	0.31	5.523	0.403
	0.219	6.281	0.259	5.803	0.249	5.636	0.259	5.695	0.219	6.233	0.218	6.085	0.254	5.405	0.241	6.250	0.2	6.595	0.254
	0.138	6.260	0.163	5.748	0.157	5.096	0.163	5.719	0.138	6.330	0.138	5.703	0.160	5.308	0.152	6.490	0.13	6.710	0.160
	-	-	-	-	-	-	-	-	0.087	4.056	-	-	-	-	0.096	5.624	0.08	5.159	0.101
	-	-	-	-	-	-	-	-	0.055	5.673	-	-	-	-	0.061	5.122	0.05	5.778	-
Area (mm <sup>2</sup> )	30.81		32.25			36.88	36.84	36.88	36.74		36.88		36.81	36.88		36.88		36.63	36.74
n	896		812			811	940	904	1150		904		733	1302		1278		1372	1372
CND (×10 <sup>11</sup> m <sup>-3</sup> )	0.268		0.231			0.231	0.288	0.288	0.390		0.272		0.198	0.470		0.457		0.508	0.508
vol.%	57.1		59.3			59	62.2	62.2	64.3		50.9		62.9	63.7		55.9		62.9	62.9
Intercept	7.76		7.18			6.87	7.07	7.07	7.5		7.37		6.58	7.69		7.96		7.84	7.84
Slope	-7.24		-5.84			-5.39	-5.53	-5.53	-6.5		-6.51		-5.04	-6.58		-7.8		-6.87	-6.87
r <sup>2</sup>	0.9661		0.9689			0.9816	0.9943	0.9943	0.9220		0.9785		0.9885	0.9558		0.9257		0.9793	0.9793



**Fig. 9** **a** Classic CSD diagram for plagioclase crystals in thin sections LS1 to LS10. There are small but significant variations between the different samples. **b** Binary image of the plagioclases in a digitized thin section (LS4). **c** Variations in the slope of CSDs (red) and the crystal number density (CND; blue) plotted across the profile through the column (from LS1 to LS10). The two graphs correlate inversely with each other, i.e., a high CND corresponds to a steep slope in the CSD diagram and the other way around. **d** Plot of CSD-slope versus measured mean orientation for plagioclase across the Hrepphólar column. Note that there is a rough correlation between slope and orientation in that samples with steeper CSD-trends have more flatly arranged laths and vice versa



80 m depth within the Holyoke flood basalt and several other locations (Philpotts and Dickson 2002 and references therein). Philpotts et al. (1998, 1999) and Philpotts and

Dickson (2000, 2002) also showed by their detailed descriptions and experimental work, that the minerals tend to form layering during cooling of a thick lava flow (i.e., such as

Hrepphólar). These layers primarily consist of plagioclase chains which begin forming during an early stage of crystallization (i.e., 75 % liquid, Philpotts and Dickson 2000, 2002; Philpotts et al. 1998, 1999). When the plagioclase chains have formed (with interstitial olivine and clinopyroxene), the remaining melt starts to crystallize titanomagnetite (as the melt is more enriched in Ti and Fe). Thus, this type of modal layering is a relatively common phenomenon in thick and slowly solidified basalt flows.

As we do not detect any systematic variations in the mineral chemistry across the column (Table 2), it is clear that we cannot use mineral chemistry in this case to substantiate or to refute any of the proposed models that explain the internal structures of basalt columns. However, it has been shown experimentally that the anorthite content of plagioclase correlates positively with the amount of H<sub>2</sub>O dissolved in a basaltic melt (Takagi et al. 2005 and references therein). Thus, assuming that constitutional supercooling (as proposed by Guy and Le Coze (1990) and Guy (2009)) and enrichment of volatiles in the central parts of the column was responsible for the observed banding we would expect to see trends of more An-rich plagioclase in the centre (at least reflected in the compositions of plagioclase microphenocrysts). This is not the case at Hrepphólar (Table 2).

Although there is no clear fractionation/accumulation path indicated by the modeling of bulk-rock compositions (Fig. 5), the data clearly suggest variability in the amount of different phenocryst phases present. Considerable scatter can be expected in this plot since the individual bulk-rock samples are relatively large (1 cm<sup>3</sup>) whereas the banding is on a significantly smaller scale (typically 0.5 mm in width). A single bulk-rock sample may thus contain several darker/brighter bands and the bulk-rock analyses represent an average of these. However, the petrological variations recorded across the A-profile (Figs. 5 and 6; Table 1) are unlikely to be simply the result of analytical scatter. The positive peaks in TiO<sub>2</sub> and Fe<sub>2</sub>O<sub>3</sub> content (oxides, and their strong covariance), coupled with negative trends in other oxides (e.g., SiO<sub>2</sub>, Al<sub>2</sub>O<sub>3</sub>, MgO, and Na<sub>2</sub>O), correlate quite well with the darker bands in the polished plate. This suggests that dark bands are related to relative enrichment of titanomagnetite, which is also supported by the petrographic observations of thin sections (Fig. 4d). Also different modal amounts of plagioclase crystals in the samples A1 to A27 can be inferred from the variation of the Eu anomaly (Eu/Eu\* = 0.913–1.092) with respect to the average composition of the Hrepphólar column.

Based on the absence of mineral assemblages characteristic for alteration (e.g., iddingsite formation in combination with crystallization of various zeolite minerals; Smedes and Lang 1955), we conclude that the Hrepphólar columns were not subject to extensive alteration and that alteration cannot

explain the observed banding. This is also supported by field observations, because alteration from the sides of the columns cannot produce the observed cross-cutting relations between bands and column-delimiting joints.

The origin of the banding within the Hrepphólar column can be inferred to be the result of systematic and repetitive enrichment/depletion of different elements in the melt as the lava slowly cools and solidifies (similar to that described by Philpotts and Dickson 2002). However, the small variations in mineralogy and geochemistry across the plate are not sufficiently clear to provide conclusive evidence for any of the three remaining models (i.e., double-diffusive convection, constitutional supercooling and crystallization induced melt migration). This has been pointed out previously by Guy (2009) who argued that it is unlikely that geochemical (and mineralogical) fingerprints of the processes will be preserved, because the minerals in a basaltic magma crystallize under relatively similar *P-T* conditions and to a large extent also during same time (i.e., overlapping crystallization sequences). Therefore, it is difficult to produce a clear geochemical trend across the columns (except for perhaps the volatile concentrations as suggested by Guy 2009). Based on the 27 bulk-rock samples analyzed by XRF and LA-ICP-MS in this study, we completely agree with Guy (2009) that geochemical analyses do not allow discrimination among the different genetic models. Alternative indicators must be sought to identify the processes responsible for the internal structures at Hrepphólar.

#### Orientation of plagioclase laths and crystal size distributions

In many subaerially emplaced basaltic lava flows, plagioclase laths are arranged sub-horizontally, reflecting the original alignment imposed during flow emplacement. This original flow-related mineral orientation can be later overprinted by mineral growth during slow cooling and crystallization in random directions after the flow has stopped moving (Smith 2002 and references therein). The plagioclase crystals at Hrepphólar have inclinations in 2D between 95° and 131° (Fig. 8), but there is some order to their orientations depending on location within the plate. In general the central part of the investigated column has more steeply oriented crystals than the rock at the plate edges (7.5 cm in from the column boundary) (Figs. 8 and 9c). This difference in mean orientation is slight but important.

It has previously been shown experimentally that rapid cooling in basaltic systems leads to steeper trends in the CSD plots (i.e., there is not a significant difference of the sizes of the individual crystals) of plagioclase for any given temperature (i.e., Burkhard 2002; Hammer 2008; Pupier et al. 2008). As the minerals in our thin sections from the Hrepphólar column do not show any systematic compositional variation with location, we can assume that the

different parts of the column crystallized under similar temperature conditions. This is also supported by the titanomagnetite–ilmenite thermometer (Sauerzapf et al. 2008), which suggests stable crystallization temperatures between 988 and 999 °C across the column. From Fig. 9a–d, it is clear that the polished slab displays steeper CSD trends towards its edges, combined with a flattening inwards. This systematic change is consistent with faster cooling at the edges of the column, creating steeper CSD trends, which means minor variation in crystal size, versus slower cooling away from the edges resulting in less steep trends and thus more variability in crystal size (i.e., in the internal parts). There are also characteristically kinked trends for some of the samples (Fig. 9a). Such trends are typically attributed to mechanical mixing of crystal populations, grown under different conditions (Higgins 2006 and references therein). Hence, the kinked trends in our samples may also arise from mixing of two separate populations of crystals: (1) one that formed early crystallizing, discontinuous, plagioclase chains (as suggested by Mattsson et al. 2011) and (2) another population of smaller plagioclase crystals which grew contemporaneously with melt migration in the column.

It also is interesting to note that there is a rough correlation between CSD slope and the mean 2D orientation of plagioclase laths (Fig. 9d). That is, samples with steeper CSD's generally display subhorizontally oriented plagioclase crystal trends. This is consistent with rapid cooling (Brugger and Hammer 2010) near the edges of the column. The flatter CSD trends recorded near the centre of the column (i.e., slower cooling) are for more steeply oriented laths. This may be interpreted as fast cooling nearer the column edges preferentially capturing plagioclase crystals in place as it was preferentially aligned during emplacement of the lava flow on a near-horizontal surface (see Smith 2002 and references therein). The internal parts of the column which cooled more slowly, display flatter CSD trends and the steeper orientation of laths of these parts of the column are indicative of internal movement (flow of melt along the main axis of the column). The textural data from Hrepphólar shows evidence only for unidirectional, upward flow and therefore we conclude that the CSD and crystal orientation data is most consistent with the crystallization-induced melt migration model proposed by Mattsson et al. (2011).

#### Origin of the diffuse and sharp banding

The origin of the two types of dark banding (diffuse and sharp) is not obvious at a first glance. The diffuse bands all show small but distinct variations in the modal proportions of phenocrysts (e.g., titanomagnetite varies between 4 and 7 modal% in the bright and dark bands respectively). Targeted microprobe analyses of the dark sharp bands, however, points to a

slightly more evolved composition of the melt. The sharp bands also contain more vesicles (up to 10 vol.%) compared with the rest of the column (typically, <5 vol.% vesicles). We interpret the sharp-edged bands to record contractional cracking during solidification of the column. As the contractional crack opens, the last liquid from the crystal framework within the column is squeezed in to fill the void. The magmatic pressure in thick lava flows should be sufficient to squeeze the last remaining liquids into cracks (i.e., 10 bar pressure at 30 m depth). Since this liquid is also enriched in volatiles compared with the bulk composition due to crystallization of the volatile-free phenocryst assemblage at Hrepphólar, vesiculation occurs as soon as the liquid enters the contractional crack (and the lower pressure therein). This interpretation also explains the crosscutting relationships of the sharper bands with the diffusive bands.

#### Additional support for unidirectional melt migration from AMS measurements

It is clear that the different models proposed to explain the internal structure in basalt columns all predict relatively minor variations the chemistry of the column. This also explains why previous attempts to find systematic compositional variations have failed (also in this study). We suggest that the most relevant information regarding the genesis of the internal structures comes from detailed petrographic studies. The combination of 2D measurements and CSDs for plagioclase, showing correlated systematic variations across the column, provides compelling evidence for unidirectional movement of the melt along the long-axis of the Hrepphólar columns. This interpretation is further substantiated in the accompanying paper, which shows the rock magnetic properties and AMS for the same column we used for the present study. In the complementary paper, Almqvist et al. (2012) report a systematic increase in single-domain titanomagnetite towards the central parts of the Hrepphólar column as well as a significant change in the shape of the magnetic susceptibility ellipsoid (showing increasingly prolate fabric towards the centre of the plate). The paramagnetic sub-fabric (e.g., olivine and clinopyroxene) varies systematically with the observed macroscopic banding in the plate whereas the principal axis of the ferrimagnetic subfabric (predominantly titanomagnetite) shows strong grouping near the vertical axis of the column. The authors interpret this to reflect vertical melt migration in the last stages of crystallization of the Hrepphólar columns.

The similar and systematic variations across the basalt column recorded by both the textural analysis (orientation measurements in combination with crystal size distributions) and the AMS-measurements (and rock magnetic properties) strongly suggest melt migration within the internal parts of the Hrepphólar columns.



## Conclusions

Our small-scale study of a plate from within a single basalt column shows that it is virtually impossible to discriminate between the different models proposed to explain internal structures in columnar-jointed basalts solely based on petrological and mineralogical variations across the column. There are, however, subtle variations that can be used to test the different models. Firstly, the deuteric alteration model can be completely ruled out for the Hrepphólar columns because they lack the mineral assemblages that are characteristic of alteration (i.e., iddingsite and/or zeolites). The internal structures of the Hrepphólar basalt columns must thus present primary magmatic features, which are corroborated by the fact that roughly 20 % of the structures observed in the field along each meter of the column axes are cut by the column-bounding fractures (i.e., the joint planes).

The consistent titanomagnetite–ilmenite crystallization temperatures (i.e.,  $994 \pm 6$  °C) across the column are also difficult to reconcile with the double-diffusive convection and constitutional supercooling models which both require distinct differences in chemical composition as well as temperature to drive the processes. If the chemical difference was mainly due to enrichment of volatiles (such as H<sub>2</sub>O) due to crystallization of an anhydrous mineral assemblage in the central parts of the column, we would expect the late-crystallizing plagioclase microphenocrysts to be more An-rich plagioclases. This is not the case at Hrepphólar. Moreover, absence of downward-warped material required to maintain convective motions are speaking against these hypotheses.

We conclude that the systematic variations of plagioclase orientations (measured in 2D in a vertical plane) and the crystal size distributions across the plate are most consistent with the crystallization induced melt migration hypothesis in which material flows from deeper parts of the lava flow into the central parts of the columns in response to the volume decrease associated with solidification. This melt migration process occurring within the columns may significantly affect the cooling rate for columnar-jointed lava flows and intrusions.

**Acknowledgments** The authors thank Bjørn Almquist and Ann Hirt for introducing the AMS technique and many interesting discussions on the magnetic fabrics of the Hrepphólar columns. The authors are also grateful to Ármann Höskuldsson for first introducing the peculiar structures inside the columns from Hrepphólar and S. Helgason Ehf. (Reykjavik) who provided the polished slab that was used for this project. Finally, Lydia Zehnder and Markus Wälle are also acknowledged for assisting with XRF and LA-ICP-MS measurements.

## References

Almquist BS, Bosshard SA, Hirt AM, Mattsson HB (2012) Internal flow structures in columnar jointed basalts from Hrepphólar,

- Iceland: II. Rock magnetic properties and magnetic anisotropy (this issue)
- Alt JC, Laverne C, Vanko D (1996) Hydrothermal alteration of a section of the upper oceanic crust in the eastern equatorial Pacific. A synthesis of results from site 504 (DSDP Legs, 69, 70 and 83 and ODP Legs 111, 137, 140 and 148). In: Alt JC, Kinoshita H, Stokking L, Michael PJ (eds). Proceedings of the ODP Scientific Results, vol. 148, pp. 417–434
- Andrews AJ (1980) Saponite and celadonite in layer 2 basalts, DSDP Leg 37. *Contrib Mineral Petrol* 73:323–340
- Boudreau AE, Philpotts AR (2002) Quantitative modeling of compaction in the Holyoke flood basalt flow, Hartford Basin, Connecticut. *Contrib Mineral Petrol* 144:176–184
- Brugger CR, Hammer JE (2010) Crystal size distribution analysis of plagioclase in experimentally decompressed hydrous rhyodacite magma. *Earth Planet Sci Lett* 300(3–4):246–254
- Budkewitsch P, Robin PY (1994) Modelling the evolution of columnar joints. *J Volcanol Geotherm Res* 59(3):219–239
- Bulkeley R (1693) Part of a letter concerning the Giants Causeway in the County of Atrim in Ireland. *Philos Trans R Soc Lond* 17:708
- Burkhard D (2002) Kinetics of crystallization: example of microcrystallization in basalt lava. *Contrib Mineral Petrol* 142(6):724–737
- Ellwood BB (1979) Anisotropy of magnetic susceptibility in variations in Icelandic columnar basalts. *Earth Planet Sci Lett* 42:209–212
- Ellwood BB, Fisk MR (1977) Anisotropy of magnetic susceptibility variations in a single Icelandic columnar basalt. *Earth Planet Sci Lett* 35:116–122
- Fritz WJ, Stillman CJ (1996) A subaqueous welded tuff from the Ordovician of County Waterford, Ireland. *J Volcanol Geotherm Res* 70(1–2):91–106
- Gill R (2010) *Igneous rocks and processes: a practical guide*. Wiley-Blackwell
- Gilman JJ (2009) Basalt columns: large scale constitutional supercooling? *J Volcanol Geotherm Res* 184:347–350
- Glicksman ME (2011) Constitutional supercooling. In: *Principles of Solidification*. Springer, New York, pp 213–235
- Goehring L, Morris SW (2005) Order and disorder in columnar joints. *Europhys Lett* 69(5):739–745
- Grossenbacher KA, McDuffie SM (1995) Conductive cooling of lava: columnar joint diameter and stria width as functions of cooling rate and thermal gradient. *J Volcanol Geotherm Res* 69(1–2):95–103
- Guillong M, Meier DL, Allan MM, Heinrich CA, Yardley BWD (2008) Appendix A6: SILLS: a MatLab-based program for the reduction of Laser Ablation ICP-MS data of homogeneous materials and inclusions. Mineralogical Association of Canada Short Course 40, Vancouver, B.C.:328–333
- Guy B (2009) Basalt columns: large scale constitutional supercooling? Comments on the paper by John Gilman (JVGR, 2009) and presentation of some new data. *J Volcanol Geotherm Res*
- Guy B, Le Coze J (1990) Reflections on columnar jointing of basalts: the instability of the planar solidification front. *C R Acad Sci Paris* 311(II):943–949
- Hammer JE (2008) Experimental studies of the kinetics and energetics of magma crystallization. *Rev Mineral Petrol* 69:9–59
- Higgins MD (2000) Measurement of crystal size distributions. *Am Mineral* 85:1105–1116
- Higgins MD (2006) *Quantitative textural measurements in igneous and metamorphic petrology*. Cambridge University Press, Oxford, p 254
- Juteau T, Noack Y, Whitechurch H (1979) Mineralogy and geochemistry of alteration products in holes 417A and 417A and 417D basement samples (Deep Sea Drilling project LEG 51). In: Donnelley T, Francheateau J, Bryan W, Robinson P, Flower M, Salisbury M

- (eds). Initial Reports of the Deep Sea Drilling Project, LI, LII:1273–1297
- Kantha L (1981) ‘Basalt fingers’—origin of columnar joints? *Geol Mag* 118:251–264
- Kristinsdóttir BD (2010) Samanburður á punktálags- og einásabrotstyrk bergsýna úr Helgúvík og Hólahnúkum. Bachelor thesis, Sigillum Universitatis Islandiae
- Kristmannsdóttir H (1979) Alteration of basaltic rocks by hydrothermal activity at 100–300 °C. In: Mortland MM, Farmer VC (eds) International Clay Conference. Elsevier, Amsterdam, pp 359–367
- Mattsson HB, Caricchi L, Almqvist BSG, Caddick MJ, Bosshard SA, Hetényi G, Hirt AM (2011) Melt migration in basalt columns driven by crystallization-induced pressure gradients. *Nat Commun* 2:299
- Michol KA, Russell JK, Andrews GDM (2008) Welded block and ash flow deposits from Mount Meager, British Columbia, Canada. *J Volcanol Geotherm Res* 169(3–4):121–144
- Mock A, Jerram DA (2005) Crystal size distributions (CSD) in three dimensions: insights from the 3D reconstruction of a highly porphyritic rhyolite. *J Petrol* 46(8):1525–1541
- Morgan DJ, Jerram DA (2006) On estimating crystal shape for crystal size distribution analysis. *J Volcanol Geotherm Res* 154:1–7
- Philpotts AR, Dickson LD (2000) The formation of plagioclase chains during convective transfer in basaltic magma. *Nature* 406:59–61
- Philpotts AR, Dickson LD (2002) Millimeter-scale modal layering and the nature of the upper solidification zone in thick flood-basalt flows and other sheets of magma. *J Struct Geol* 24:1171–1177
- Philpotts AR, Shi J, Brustman CM (1998) Role of plagioclase crystal chains in the differentiation of partly crystallized basaltic magma. *Nature* 395:343–346
- Philpotts AR, Brustman CM, Shi J, Carlson WD, Denison C (1999) Plagioclase-chain networks in slowly cooled basaltic magma. *Am Mineral* 84:1819–1829
- Pupier E, Duchene S, Toplis M (2008) Experimental quantification of plagioclase crystal size distribution during cooling of a basaltic liquid. *Contrib Mineral Petrol* 155(5):555–570
- Rasband W (2008) ImageJ 1.41o Image Processing and Analysis in Java, Computer software. In: National Institutes of Health, USA
- Saemundsson K (1970) Interglacial lava flows in the lowlands of Southern Iceland and the problem of two-tiered columnar jointing. *Jökull* 20:62–77
- Sauerzapf U, Lattard D, Burchard M, Engelmann R (2008) The titanomagnetite–ilmenite equilibrium: new experimental data and thermo-oxybarometric application to the crystallization of basic to intermediate rocks. *J Petrol* 49(6):1161–1185
- Schenato F, Formoso MLL, Dudoignon P, Meunier A, Proust D, Mas A (2003) Alteration processes of a thick basaltic lava flow of the Paraná Basin (Brazil): petrographic and mineralogical studies. *J S Am Earth Sci* 16(5):423–444
- Shelley D (1993) Igneous and metamorphic rocks under the microscope. Chapman and Hall, London, p 445
- Smedes HW, Lang AJJ (1955) Basalt column rinds caused by deuteric alteration. *Am J Sci* 253:179–181
- Smith JV (2002) Structural analysis of flow-related textures in lavas. *Earth Sci Rev* 57(3–4):279–297
- Spry A (1962) The origin of columnar jointing, particularly in basalt flows. *Aust J Earth Sci* 8(2):191–216
- Sun SS, McDonough WF (1989) Chemical and isotope systematics of oceanic basalts: implications for mantle composition and processes. In: Saunders AD, Norry MJ (eds) *Magmatism in the Ocean Basins*. Spec Publ Vol Geol Soc London 42:313–345
- Takagi D, Sato H, Nakagawa M (2005) Experimental study of a low-alkali tholeiite at 1–5 kbar: optimal condition for the crystallization of high-An plagioclase in hydrous arc tholeiite. *Contrib Mineral Petrol* 149(5):527–540
- Tomkeieff SI (1940) The basalt lavas of the Giant’s Causeway district of Northern Ireland. *Bull Volcanol* 6:89–146
- Turner JS (1973) *Buoyancy effects in fluids*. Cambridge University Press, Oxford
- Wright TL, Okamura RT (1977) Cooling and crystallization of tholeiitic basalt, 1956 Makaopuhi lava lake, Hawaii. *U S Geol Surv Prof Pap* 1004:78